Optical 3D-Nanometry to Study the Function of Biomolecular Motors in Nanotransport

Dissertation

zur Erlangung des akademischen Grades
Doktoringenieur
(Dr.-Ing.)

vorgelegt
an der Fakultät Maschinenwesen
der Technischen Universität Dresden
von

Dipl.-Kfm. Bert Nitzsche, MSc

2008

1. Gutachter: Prof. Dr. rer. nat. habil. Wolfgang Pompe

2. Gutachter: Prof. Dr. Jonathon Howard

3. Gutachter: Dr.ir. Erwin J. G. Peterman

Eingereicht am: 08.09.2008

Verteidigt am: 18.12.2008

Contents

List of Abbreviations

2-D	two-dimensional
3-D	three-dimensional
ATP	adenosine triphosphate
BME	β-mercaptoethanol
BRB	Brinkley reassembly buffer
CCD	charge-coupled device
DMSO	dimethyl-sulfoxide
DTT	dithiothreitol
EGTA	ethylene glycol-bis (2-aminoethylether)-N,N,N',N'-tetra acetic acid
FLIC	fluorescence interference contrast
fps	frames per second
GMP-CPP	guanylyl (a,b)methylenediphosphonate
GTP	guanosine triphosphate
MAP	microtubule-associated protein
MES	2-(N-Morpholino)ethanesulfonic acid
NA	numerical aperture
ncd	non-claret disjunctional
PIPES	piperazine-N,N'-bis-(2-ethanesulfonic acid)
PSF	point spread function
QD	quantum dot

1 Scope and Aim

The one-hundred-thousandth part of the diameter of a human hair or one nanometer – this unit became very popular in the 1990s when nanotechnology got ready to take off. Certainly a crucial milestone back then was the book 'Nanosystems, Molecular Machinery, Manufacturing and Computation' [1] by American engineer Eric Drexler. With this book Drexler was the first one who performed a detailed technical analysis of the possibilities and limits of a visionary nanotechnology called molecular manufacturing. More than 15 years later the vision is very lively proven by the compilation of the 'Technology Roadmap for Productive Nanosystems' [2] which is a collective effort of well-renowned scientists dedicated to the idea of molecular manufacturing.

The ultimate goal of nanotechnology in the sense of molecular manufacturing is the ability to build nanoscopic as well as macroscopic structures with atomic precision by the use of nanoscopic machines working highly parallel. Unfortunately, currently it is not even predictable when this goal may be achieved - the problem is just too complex. Even though a number of man-made nanomachines, like nanocars or nanoelevators [3, 4], have been developed, they are not much more than proof-of-principle studies. However, a great number of nanomachines that self-organize to accomplish complex and specific tasks already exist in nature. As molecular machines in living cells they have been optimized through evolution for billions of years. It is only consequent that scientists have identified the potential of biological molecules to be part of molecular manufacturing or at least of preliminary nanodevices towards man-made nanomachines.

One type of sophisticated biomolecular machines are motor proteins that move along filamentous tracks of the cytoskeleton and transport cargo in living cells. The vision is to make them do likewise in engineered environments since transport of cargo is one of the fundamental problems in molecular manufacturing.

To employ motor proteins for effective, well-controlled transport applications on the nanoscale, their behavior in engineered environments needs to be understood. One important aspect is the path that motor proteins choose on the surface of cytoskeletal filaments (i.e. actin filaments and microtubules). In two dimensions (2-D) this has been studied in detail by nanometer tracking of motor-coated microbeads [5, 6], motor-attached quantum dots (QDs) [7, 8] or single fluorescently-labeled motors [9-11] moving along cytoskeletal filaments.

However, cytoskeletal filaments are three-dimensional (3-D) nanostructures on whose surface motor proteins can move on non-linear trajectories. This has severe implications in so-called 'gliding assays', a setup where the filaments are propelled by substrate-attached motor proteins in a way reminiscent of crowd surfing. In this geometry, motors that do not move parallel to the axis of the cytoskeletal filament will induce axial motion of the filament. Such an effect is of great relevance since gliding assays are most promising for nanotransport applications in synthetic environments [12, 13] where gliding filaments are envisioned to act as nanoshuttles capable of controlled cargo pick-up, transport and delivery [14, 15]. In this respect, filament rotation can be foreseen to potentially impact the movement of filament-shuttles during cargo transport.

Previous studies of motor proteins based on gliding assays have shown (i) a right-handed torque component of heavy-meromyosin onto actin filaments [16], (ii) the movement of kinesin-1 along the axis of microtubule protofilaments [17] and (iii) the presence of off-axis powerstrokes in the motion of 22S and 14S axonemal dynein [18, 19], ncd [20], and monomeric kinesin-1 [21]. In order to detect such rotations, supercoiling of actin filaments [16] and microtubules [19], or periodic sideways deflections of distinctive microtubule structures (artificial kinks or axoneme fragments) [17, 18, 20, 21], were imaged by optical microscopy. However, the experiments relied on the deliberate construction of impaired gliding assays or defective filaments and exhibited limited accuracy with respect to the quantification of rotational periodicities. Thus, the approaches of these

studies are not ideally suited to characterize nanotransport systems based on gliding cytoskeletal filaments.

It was therefore the first major goal to establish and characterize a versatile technique that is suited to characterize nanotransport systems with high precision but low impact in 3-D. The second major goal was to then apply the developed method to measure how certain types of motor proteins handle microtubules that act as nanoshuttles under various conditions.

While this work aims to contribute to the development of future nanotechnology in the sense of molecular manufacturing, the strategy to tackle the problems raised above already involves currently available nanotechnology. This present nanotechnology is used to produce and apply new, mainly chemically synthesized materials with nanometer-sized features and frequently spectacular properties. Prime examples are the treatment and structuring of surfaces, the application of nanoscopic assays and the use of fluorescent semiconductor nanocrystals – all examples without which this work would not have been possible. In this sense, today's nanotechnology is contributing to develop the nanotechnology of tomorrow and not to forget significantly contributes to the study of biological machines, which are not yet fully understood.

2 Background

2.1 Biomolecular Motors – Molecular Machines Inside Cells

2.1.1 Microtubules

Cells feature a remarkable system called 'cytoskeleton', which allows them to be shaped correctly, to organize their internal contents dynamically, and to withstand stress and strain [22]. It consists of three types of filamentous structures: (i) actin filaments, (ii) microtubules, and (iii) intermediate filaments. The actin cytoskeleton and microtubules have also been found to be involved in intracellular transport in multiple ways [22-24]. In particular, they serve as tracks for motor proteins, which carry cargo in a directed manner inside cells.

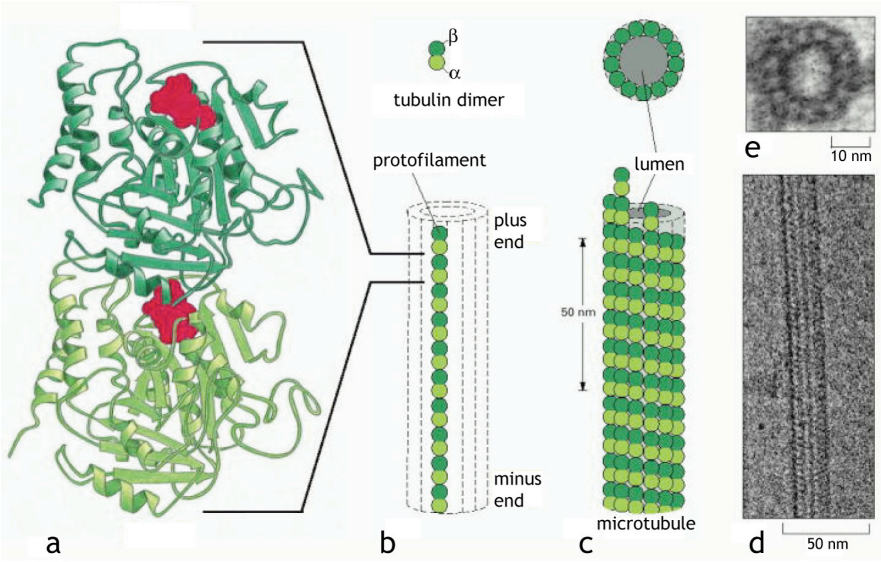

Figure 1: Microtubule structure – from tubulin to tubes. The basic building blocks of microtubules are tubulin dimers **(a)** which assemble head to tail, to form protofilaments **(b)**. Parallel alignment of the protofilaments forms closed hollow tubes - the microtubules **(c)**. Electron micrograph of microtubule segment **(d)** and cross section **(e)**. Figure adapted from [22].

The most rigid and structurally complex of the cytoskeletal filaments are microtubules. They form hollow tubes with an outer diameter of about 25 nm (Figure 1). They are composed of 8 nm long heterodimeric tubulin proteins with α- and β-tubulin monomers as basic building blocks. Tubulin dimers assemble head-to-tail thereby forming periodic strings called protofilaments. The lateral arrangement of protofilaments results in tubulin sheets, which upon closure form microtubules with a structural polarity. On account of this polarity, microtubules are terminated by α-tubulin at their so-called minus-end and β-tubulin at their plus-end. Usually, microtubules comprise 13 protofilaments *in vivo*. However, microtubules with protofilament numbers ranging from 8 to 20 have also been observed *in vivo* [17, 25].

The number of protofilaments of a microtubule is a critical parameter in the sense that it determines the exact shape of the microtubule lattice (Figure 2). This is because protofilaments are not exactly aligned side by side but rather laterally offset by ~0.9 nm. The consequence is a transverse left-handed helical arrangement of the tubulin monomers. Microtubules with 13 protofilaments display a total offset of exactly 3 tubulin monomers (or 1.5 dimers) per complete turn of the transverse helix.

In contrast, for the other occurring protofilament numbers, the total lateral offset of a full turn of the transversal helix does not coincide with a multiple of the tubulin monomer length. The resulting mismatch is taken up by an overall rotation of the microtubule lattice generating superhelices or supertwists of protofilaments. In other words, if microtubules consist of 13 protofilaments, these run parallel to the longitudinal microtubule axis, whereas in the other cases protofilaments form superhelices. The orientation of the supertwist can be right-handed (e.g. 12 protofilament microtubules) or left-handed (e.g. 14 protofilament microtubules).

Considerations of microtubule fine structure become greatly important when reconstituting microtubules. The protofilament number and thus the lattice structure of *in vitro* assembled microtubules has been reported to critically depend on the used assembly conditions [17, 26, 27]. On the one hand, this has to be kept in mind when interpreting experimental results

where the shape of the microtubule lattice is important. On the other hand, the systematic generation of certain microtubule structures can help to explore phenomena related to microtubule structure. In the course of this work, implications of the structural diversity of microtubules and its control will be discussed, specifically focusing on the application of microtubules in bionanotechnology.

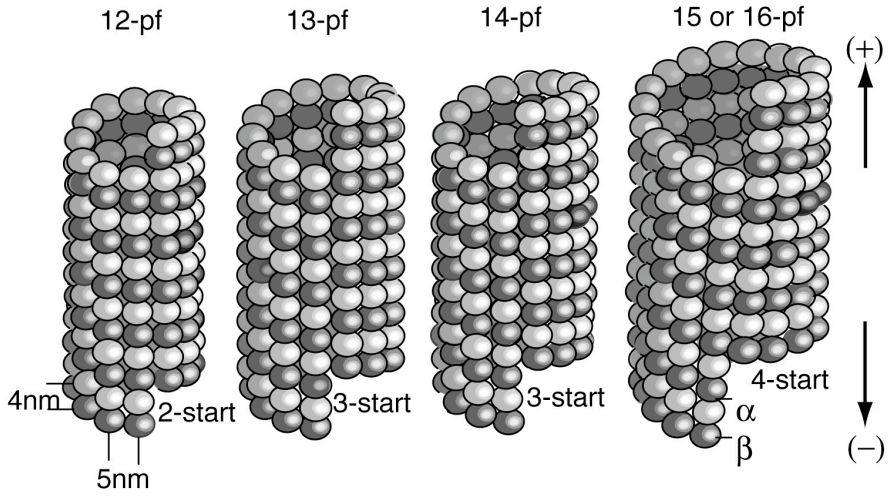

Figure 2: Varying microtubule structure for microtubules with 12 to 16 protofilaments. Protofilaments run straight when 13 of them make up a microtubule. Otherwise the lateral offset between tubulin dimers causes a mismatch, which has to be taken up by lattice rotation to form a closed cylinder. Figure adapted from [28].

The *in vivo* assembly, disassembly, and stabilization of microtubules are very dynamic processes, and have been shown to be facilitated by guanosine triphosphate (GTP) hydrolysis [29] as well as by a variety of microtubule-associated proteins (MAPs) [28, 30]. For *in vitro* applications, robust microtubules of a fixed length are usually desired. In particular, different strategies to suppress the shrinkage of dynamic microtubules have been developed. Firstly, microtubules can be stabilized by taxoids (e.g. taxol), a class of chemotherapeutics from cancer therapy. Secondly, assembly of microtubules in the presence of guanylyl (a,b)methylenediphosphonate (GMP-CPP), which is a slowly-hydrolyzable GTP-analogue, also produces

stable microtubules. Thirdly, certain MAPs like doublecortin are capable of stabilizing microtubules *in vivo* and *in vitro* [28].

2.1.2 Microtubule Motors and *In Vitro* Motility Assays

Most kinds of movement in the cellular world are generated by biomolecular motors - stunning tiny machines that have been engineered by nature. What makes them particularly fascinating is that they work unlike man-made machines, because they directly convert the chemical energy of adenosine triphosphate (ATP) by hydrolysis into mechanical energy [23, 24].

Microtubule motors are one class of motor proteins (besides actin motors) which move along filaments of the cytoskeleton, thus being referred to as linear motors. These motors have been demonstrated to be directly involved in a number of key processes in cells like meiosis, mitosis, beating of cilia and flagella, nuclear oscillations, and intracellular transport. They bind in an oriented manner to microtubules, thereby recognizing the structural polarity of their tracks. That way microtubule motors are enabled to move in a directed manner targeting either the microtubule plus or minus-end.

Studying how motors of the cytoskeleton work on the single molecule level, has mainly been facilitated by advances in optical microscopy and the invention of *in vitro* motility assays [23]. Based on their geometry, two types of *in vitro* motility assays can be distinguished: the bead assay (also called stepping assay) and the gliding assay (Figure 3). In the bead assay microtubules are immobilized on a substrate surface. The addition of a solution, which contains motor-coated beads and ATP, allows the beads to find the microtubules, bind to them, and move along their lattice. The gliding assay is built upon the inverse geometry. Here, motor proteins are attached to the substrate surface such that the motor heads are free in solution. Upon addition of microtubules and ATP, microtubules diffuse towards the surface, bind to the immobilized motors, and are translocated over the substrate surface.

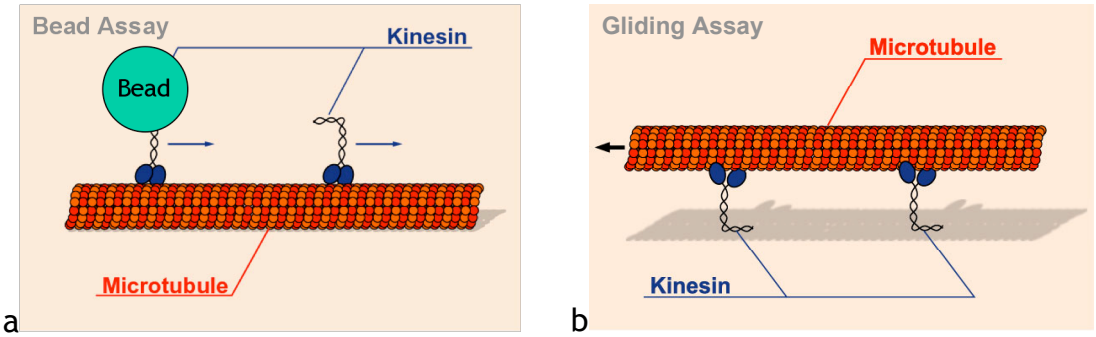

Figure 3: *In vitro* motility assays. (a) In a bead assay (also denoted stepping assay) microtubules are immobilized on a substrate surface. Motors that may have a bead bound to them diffuse in solution and bind to the microtubules where they move on the microtubule lattice. Kinesin-1 moves towards the microtubule plus-end. **(b)** In a gliding motility assay motor proteins are immobilized on the substrate surface and expose their head domain towards the solution. Microtubules diffuse in the solution and when being in close proximity to the surface eventually bind to the motors. Microtubules are then propelled by the ATP-hydrolyzing motors. In the case of kinesin-1 the microtubule minus-end is leading.

Owing to the power of *in vitro* motility assays, key properties like direction of movement, speed of movement, processivity (i.e. the length of walked distance without detaching from the microtubule), force-velocity relation, and step size have been determined for a variety of motor proteins. Following, the main characteristics of those three types of microtubule motors that were used to acquire the data presented in this work, are introduced. In particular, these are kinesin-1, 22S axonemal dynein, and the kinesin-14 non-claret disjunctional (ncd).

Kinesin-1 is one of the best understood molecular motors. It is involved in fast anterograde axonal transport [31]. The actual motor without associated light chains is a homodimer with two identical N-terminal catalytic cores (the motor 'heads') that are connected by a coiled-coil neck region [32]. The neck is followed by a rodlike stalk domain and a short C-terminal tail domain [33]. Structural studies have shown that the contour length of kinesin-1 is ~60 nm [33-35]. The motor moves towards the plus-ends of microtubules. It is doing so in 8 nm steps [6], which correspond to

the length of a tubulin dimer. Kinesin-1, which consumes 1 ATP molecule per step [36, 37], is moving in a processive manner for about 100 steps [38, 39] by a hand-over-hand mechanism [11, 40-42]. The force it can exert as a single molecule is ~6 pN [43-45]. Furthermore, kinesin-1 has also been shown to follow the protofilament axis of microtubules with high fidelity [5, 17].

Axonemal dynein was discovered more than 40 years ago [46]. However, in comparison to kinesin-1, which was found only in 1985 [47-49], it still remains much less well characterized. This has mainly been due to difficulties to produce wild type and genetically modified dynein in an expression system, as is commonly done for other motor proteins. The main reason for experimental difficulties is that dyneins are huge, i.e. 1 to 2 MDa, and have a complex subunit structure, whereas the size of most other microtubule motors is in the range of 100 kDa. Specifically, 22S dynein comprises three heavy chains, each having a size of ~500 kDa. A heavy chain consists of a head comprising six AAA (ATPases associated with diverse cellular activities) domains, a stem, and a stalk that binds to microtubules [50]. *In vivo*, axonemal dynein causes the bending of microtubules and thereby the beating of flagella and cilia [22]. Unlike kinesin-1, dyneins move towards the microtubule minus-end. Velocities of axonemal dynein *in vitro* [18, 19, 51-53] are about 10 µm/s, an order of magnitude higher than for cytoplasmic dynein [54, 55] and kinesin-1 [37, 39]. So far stepping has mainly been analyzed for cytoplasmic dynein and is still controversially discussed. In contrast to kinesin-1, load dependent variable step sizes of 8 nm and multiples of 8 nm have been reported for cytoplasmic dynein. Under low load conditions step sizes were predominantly 24 and 32 nm [56]. However, others have observed exclusively 8 nm steps [55, 57] or predominantly 8 nm steps [8] under low load. In the case of axonemal dynein, one study reports processive movement of 22S dynein with 8 nm steps, however, only at ATP concentrations below 20 µM [58]. In contrast to kinesin-1 there is also evidence that the different forms of dynein do not follow protofilaments on the microtubule lattice but rather perform off-axis steps as well [8, 18, 19].

Ncd, which is a dimeric kinesin-14, has been discovered in 1990 [20, 59]. Like dynein, it is a minus-end-directed motor [20, 59]. Unlike kinesin-1, ncd is a C-terminal motor, meaning that its catalytic core is located at the C-terminus. Another distinct feature of this motor is its second ATP-insensitive microtubule binding site, located at the N-terminus [60, 61]. *In vivo* studies have shown that ncd is required for proper meiotic and mitotic chromosome segregation, playing an important role in spindle pole organization in *Drosophila melanogaster* [62-64].

When the *in vitro* motor activity of ncd was reported [20], the speed in gliding motility assays, it translocates microtubules with, has been found to be about an order of magnitude lower than for kinesin-1 and cytoplasmic dynein. Most of the evidence reported so far has favored the hypothesis that ncd moves in a non-processive manner [65-67]. However, processive runs of ncd *in vitro* have been reported only recently [68]. Similar to dynein there is evidence that ncd powerstrokes have an off-axis component with regard to microtubule protofilaments [20].

2.2 Bionanotechnology – Utilizing Nature's Treasures

Rapid technological developments have paved the way - but also created the need - for nanotechnology. On the one hand, new tools and techniques like atomic force microscopy, scanning tunneling microscopy, and electron beam lithography have made it possible at all to understand and manipulate structures and processes on the nanoscale, i.e. on a molecular or even atomic level. On the other hand, the ever-growing complexity of electronic and mechanical devices drives the need for miniaturization and integration.

Historically, a first step has been microtechnology, where mechanical, electronic, and fluidic devices are downsized to the micrometer scale and integrated in so-called microelectromechanical systems (MEMS). The core technology that made their production possible is photolithography. The next consequent step has been further downsizing to the nanometer level towards the development of nanoelectromechanical systems (NEMS).

However, conventional production methods fail if manipulation of nanoscale structures and fabrication of nanodevices are required in a highly parallel fashion. Production facilities cannot simply be downscaled since physical principles govern the nanoworld differently [1, 23]. Therefore, the vision of molecular manufacturing was born. Molecular manufacturing is an anticipated technology that enables the creation and manipulation of nanoscopic and macroscopic objects from molecular building blocks with atomic precision by the use of nanoscopic machines. However, this technological goal cannot be achieved using currently available technology. In order to bridge the gap between current technology and the envisioned machinery for molecular manufacturing, the combination of two approaches has been proposed: (i) **top-down**, where large devices are utilized to create smaller and more precise ones and (ii) **bottom-up**, where nanoscale structures are created and manipulated from molecular components by principles of molecular recognition and self-assembly [1].

The implementation of an advanced bottom-up approach, which already resembles the idea of molecular manufacturing to a great extend, can be found in biology. A living cell contains thousands of different molecular machines (mainly proteins) that work in a concerted, highly specific, and exquisitely precise manner. These machines allow cells to develop, differentiate, divide, and eventually die in a controlled way. Furthermore, cellular machinery provides the basis to achieve such delicate tasks as sensing and responding to the environment, converting energy from light or food into chemical energy, directed movement, and replicating the entire cellular system. Living cells can therefore be regarded as extremely complex and efficient molecular factories that are run by sophisticated nanomachines. Currently, human technology is far away from constructing similarly complex devices [13].

A major advantage of cellular machines lies in their availability, providing the basis for exploiting their potential for nanotechnology tasks. This potential is exhibited by a set of key features [69]:

1. They are nanometer-sized, i.e. they have the same size as the structures they are supposed to process. Thereby, the problem of

'big fingers', associated with extremely space-occupying macroscopic machinery, can be avoided and highly parallel manipulation of structures becomes possible.

2. They are extremely specific and recognize interaction partners with high fidelity. Thereby, undesired crosstalk between different functions can effectively be avoided.
3. They are remarkably energy efficient, for they directly convert chemical energy into mechanical work. Motor proteins like kinesin-1 and F1-ATPase can achieve efficiencies of 50 % [23] and even close to 100 % [70-72], respectively. In contrast macroscopic combustion engines currently used in cars convert chemical energy into heat before converting the heat into mechanical work. They only achieve efficiencies up to 35 %.
4. A large variety of genetic engineering tools makes it possible to produce them easily and even to modify and tailor their function.
5. They are cheap. Billions of protein molecules can be produced for less than one Euro-cent and industrial up-scaling of production would further reduce costs.
6. As natural components of cells they are biocompatible, which is a major advantage for potential medical applications.

One class of biomolecular machines that fulfill mechanical tasks and in particular facilitate cargo transport inside living cells are motor proteins of the cytoskeleton (see Chapter 2.1.2). Certainly, it seems obvious to also use cellular motors for nanotransport in engineered environments with applications in sorting, purification, or assembly of materials [12, 73]. Towards this goal, *in vitro* motility assays (see Chapter 2.1.2) play an equally important role as they have already done for studies of motor protein dynamics. They have turned out to be extremely valuable for designing and studying nanotransport systems, where cargo is envisioned to be transported between defined locations by molecular shuttles in a controlled fashion (Figure 4).

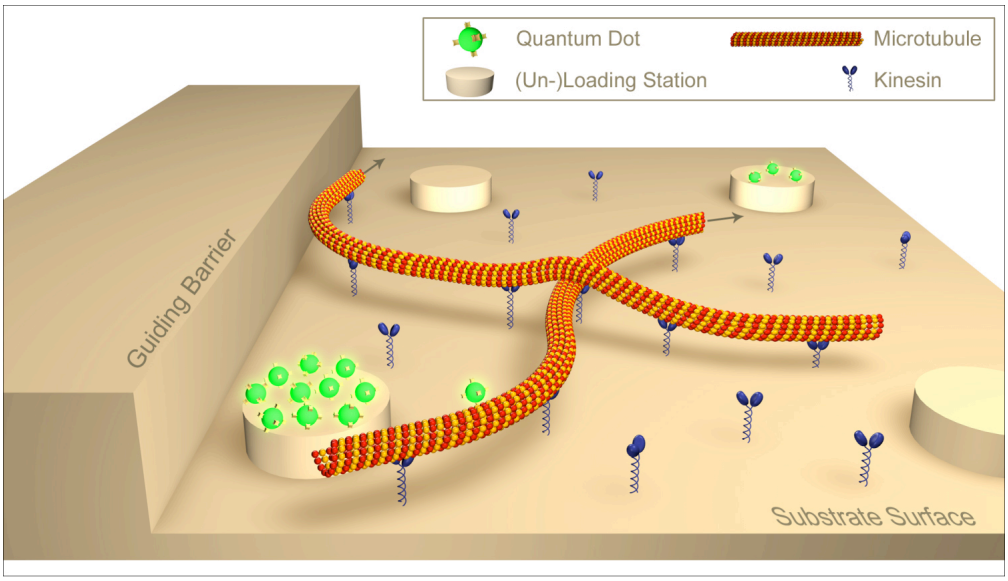

Figure 4: Illustration of a nanotransport system based on molecular motor systems. Microtubules are acting as nanoshuttles. Based upon the geometry of a gliding motility assay they can pick up and bind cargo (e.g. QDs) at defined loading stations via specific interactions of adapter-molecules (e.g. biotin-streptavidin). Shuttles are guided by appropriate means (e.g. barriers) and the transported cargo is translocated to its desired destination, where it is dropped off.

The major challenge that has to be addressed is to temporally and spatially control the motion of nanoshuttles as well as the loading and unloading of cargo. Towards this goal the geometry of the gliding motility assay has emerged to be favored [13]. One reason is that in the bead assay geometry the filaments that serve as tracks have to be accurately positioned and aligned, which is technically challenging. In contrast, the filament shuttles in gliding motility assays can move freely, i.e. guiding is not generally restricted to pre-existing routes. In addition, the filament shuttles can exert large forces (>>10 pN), since high numbers of motors can drive them collectively, offer a large surface to transport cargo, and are easier to functionalize than single motor proteins. In recent years numerous methods have been developed to control nanotransport based on motor proteins [13, 74]. For the guiding of nanoshuttles such different principles as chemical [75], topographical [76, 77], or biotemplate-assisted [78] surface

structuring, or the application of electric [79], magnetic [80], or hydrodynamic flow fields [81] have been taken advantage of. Another area of nanotransport control includes the reversible starting and stopping of motility and has been achieved by using the slowly hydrolysable ATP-analogue adenylyl-imidodiphosphate [82], or photo-inducible caged ATP [76, 83]. Alternatively, thermo-responsive polymers have been employed to control microtubule binding to motor-coated surfaces [84]. The handling of cargo in particular cargo pick-up [14] and delivery [15] are important subjects of current research as well. Reports on the transport of a variety of cargoes including polystyrene beads [76], DNA molecules [85, 86], QDs [87], and virus particles [88] illustrate the potentially broad applicability of nanotransport systems.

Although there are many promising approaches how to master nanotransport, a detailed knowledge about the exact behavior of the nanoshuttles with and without cargo bound, is still one prerequisite of effective control. For example it has been observed that microtubules may move in circular vortices on a surface, which is randomly-coated with flagellar dynein [89]. It has further been demonstrated that microtubules may rotate around their longitudinal axis upon forward movement in gliding motility assays [17, 18, 21]. For non-processive kinesin-1 monomers the suppression of these rotations by a long lever structure at microtubule ends had no effect on the speed of the forward movement [21]. If one really wants to understand such effects, and accordingly employ, support or avoid them, further studies on how motor proteins exactly move under certain conditions on the microtubule lattice are indispensable.

2.3 2-D Nanometer Tracking

In order to understand how proteins work on a single molecule level, we have to apply techniques, which reveal information about their structure and their dynamic properties. In fact, numerous techniques like electron microscopy (EM), x-ray crystallography, small angle x-ray scattering, and atomic force microscopy (AFM) have been developed to meet this demand.

They are capable of providing molecular or even atomic detail of objects, and have helped to gain valuable insight into the structure of proteins. However, the quoted techniques either demand samples to be fixed, physically perturb the molecules of interest or rely on bulk measurements. For these reasons they are not suited for the observation of the dynamics of single molecules. An extremely powerful alternative approach in this respect is optical microscopy, since it works with visible light, which has low impact on the samples to be observed. Optical microscopy has for example been widely used in the form of brightfield, darkfield, differential interference contrast, and fluorescence microscopy to study biological specimen [22].

Unfortunately, owing to diffraction, the spatial resolution of optical imaging is not arbitrary. This has been described, as early as in the 1870s, by Ernst Abbe and Lord Rayleigh for coherent and incoherent imaging, respectively. In both cases a resolution limit of ~200 nm applies, which is roughly half of the wavelength of the light used for imaging. Given the dimensions of proteins of a few nanometers (see Chapter 2.1 for the example of motor proteins and microtubules) this is absolutely insufficient if one wants to understand how single molecules interact or to even study intramolecular changes.

Nevertheless, with 2-D tracking there is a further optical microscopy based technique that does not suffer from the resolution limit. Provided that there is a single point source in the image, the center of its optical transfer function – the so-called airy disc - can be approximated very accurately by 2-D Gaussian fitting [90-93]:

$$G(x;y) = A\exp\left[-\frac{(x-x_0)^2}{2\delta_x^2} - \frac{(y-y_0)^2}{2\delta_y^2}\right], \qquad \text{(Equation 1)}$$

where A denotes the amplitude of the signal, x_0 and y_0 constitute the center of the function, and δ_x and δ_y are the standard deviations of the Gaussian in x- and y-direction, respectively.

In consequence the position of an object can be tracked with an accuracy that is two orders of magnitude better than the actual resolution limit. Even though there is also a fundamental limit for single molecule localization [94], in practice 2-D Gaussian tracking has been proven to be capable of providing precision around 1 nm. It has successfully been applied in order to study the dynamics of single molecules, one major example being motor proteins of the cytoskeleton [10, 95]. The main parameter that controls noise and thereby tracking accuracy is the number of photons captured by a charge-coupled device (CCD) camera [93]:

$$\delta_i = \sqrt{\frac{s_i^2}{N} + \frac{a^2}{12N} + \frac{8\pi s_i^4 b^2}{a^2 N^2}}, \qquad \text{(Equation 2)}$$

where s_i denotes the standard deviation of the distribution that corresponds to the Gaussian fit function (*i* refers to the x- and y-dimensions), *N* denotes the number of collected photons (background corrected), *a* denotes the pixel size, and *b* denotes the background noise.

In the order that is given in the equation, the three summands in the square root correspond to (i) photon shot noise, (ii) pixilation noise, and (iii) background noise. All three individual sources of noise inversely scale either with the square root of the number of collected photons or with the number of collected photons itself.

The approach of Gaussian fitting of optical transfer functions has even been extended to break the resolution limit of conventional optical microscopy. The according techniques are called photo-activated localization microscopy (PALM) [96] and stochastic optical reconstruction microscopy (STORM) [97]. In both methods, an imaging area contains many photoactivatable fluorophores and part thereof gets stochastically photoactivated by a light pulse and imaged subsequently. Since only a few fluorophores are activated at a time, they are well separated and can be localized by Gaussian fitting. After the fluorophores get photobleached a new pulse of light is applied to repeat the photoactivation and so on. In this way, fluorescent images can be sequentially reconstructed which by far surpass the resolution of conventionally acquired fluorescence images.

However, the cost of the fantastic resolution is a low imaging rate, making an application for studying protein dynamics impossible.

2.4 3-D Nanometer Tracking

When applying 2-D nanometer tracking to study how molecular machinery works *in vivo* and *in vitro* the achieved understanding will always remain incomplete, since the molecules operate in 3-D space. That is why the development of 3-D nanometer tracking has been a crucial step. The problem is to find a technique where it is possible to combine the above described 2-D tracking with an additional way to measure height information. One approach that has recently been applied to study the behaviour of molecular motors is 3-D tracking based on dual-focus imaging [98, 99]. While this approach is capable of nanometer resolution in 3-D, it is technically demanding and requires a sophisticated microscope setup. An alternative approach, which delivers similar sensitivity, is the combination of 2-D nanometer tracking with height measurements based on fluorescence interference contrast (FLIC) microscopy [100, 101].

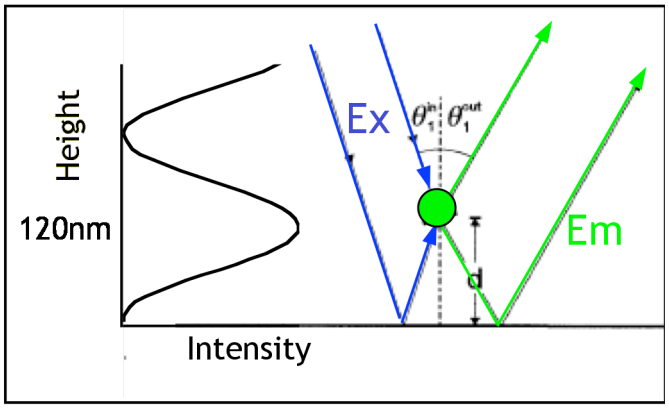

Figure 5: Principle of FLIC microscopy on a reflective surface. A fluorophore is being excited by direct and reflected light. Depending on its height above the surface there will be interference of both components. Likewise, fluorescent emission has a direct and a reflected component. In consequence, a periodic modulation of detected fluorescence intensity as a function of height above the surface can be observed in the vicinity of the surface.

FLIC microscopy is being performed in the vicinity of a reflective substrate surface. A fluorophore above the surface may be excited by direct light as well as by reflected light (Figure 5). The direct light interferes with the reflected light and causes standing waves. Therefore, the excitation of the fluorophore will depend on its position with respect to the reflecting surface. The same is true for the light emitted by that fluorophore. In consequence, a periodic modulation of detected fluorescence intensity as a function of height above the surface can be observed in vicinity of the surface. Assuming roughly identical wavelengths of excitation and emission wavelengths in the order of 600 nm, the periodicity of the intensity modulation is expected to be ~230 nm [101]. In other words, the first maximum of the FLIC intensity curve will appear 100 – 150 nm above the reflecting surface. FLIC microscopy has been proven to be capable of nanometer resolution and - unlike other 3-D nanometric approaches – of measuring absolute height values above the surface [101]. Particularly to achieve the latter careful and labor-intensive calibration of the imaging system is required. However, even without exact calibration of the imaging system, relative height variations can very easily be directly derived from changes in fluorescence intensity. Beyond this, also in terms of instrumentation, FLIC microscopy is a very straight forward and easy to establish approach. In fact, a standard epi-fluorescence microscope is sufficient to effectively use the potential of FLIC microscopy. Illumination can be accomplished by the use of an arc lamp or a laser. The only requirement is that experiments have to be performed on reflective substrates like silicon wafers commercially available at low cost.

2.5 Quantum Dots as Fluorescent Labels

Fluorescent semiconductor nanocrystals also known as quantum dots (QDs) are a prime example of how nanotechnology and thereby created nanomaterials can be applied in order to study biological systems [102-104]. They are made from semiconductor materials like cadmium sulfite (CdS), cadmium selenide (CdSe), or cadmium telluride (CdTe) and can be used to

overcome limitations like photobleaching and limiting brightness that go along with the use of conventional fluorophores be it chemical dyes or fluorescent proteins (Figure 6). QDs emit at sharply defined wavelengths, which depend primarily on QD size. In contrast, the excitation spectrum is very broad and ranges from UV up to closely below the emission wavelength (see Figure 6b). This is a feature, which cannot be underestimated as a single wavelength of incident light is sufficient to excite QDs of different colors. Moreover, high extinction coefficients (one to two orders of magnitude higher than for chemical dyes or fluorescent proteins) and quantum yields make them very bright fluorescent labels that are ideally suited for single molecule imaging. Finally, the superior photostability of QDs guarantees long life times in fluorescence imaging. Yet there is also a drawback in that QDs exhibit strong blinking behavior on various time scales ranging from sub-milliseconds to many seconds. In practice, the blinking behavior of commercially available QDs can vary a lot. This may be improved by better control of the production process in the future. Although so far there is no way to eliminate blinking completely, it has been reported that the use of the reducing agents β-mercaptoethanol (BME) and dithiothreitol (DTT) reduces blinking dramatically [105].

The pure semiconductor nanocrystals cannot be used to directly label biological probes. They rather constitute the core of QD composites (Figure 6a), which are designed to specifically bind to objects of interest. The core is capped by a transparent passivating shell, in order to prevent an oxidation-induced loss of the fluorescence properties. Building upon the passivating shell, another layer consisting of a polymer coating, tunes the solubility of the QD composites in aqueous solutions and provides the basis for conjugation to bioactive molecules like antibodies or streptavidin.

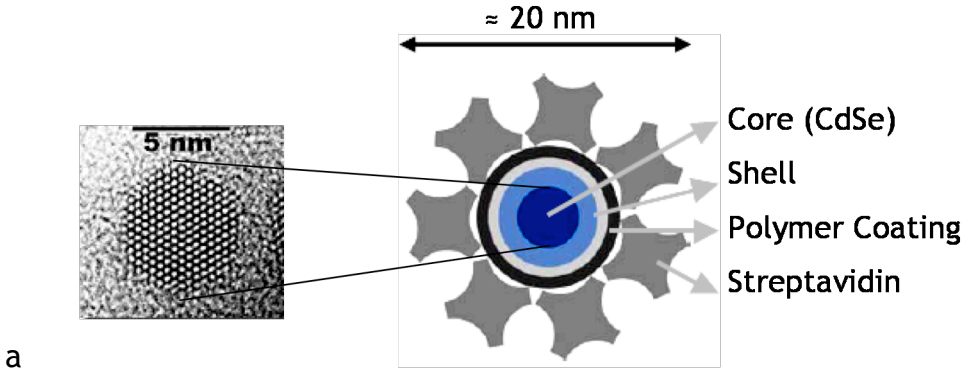

a

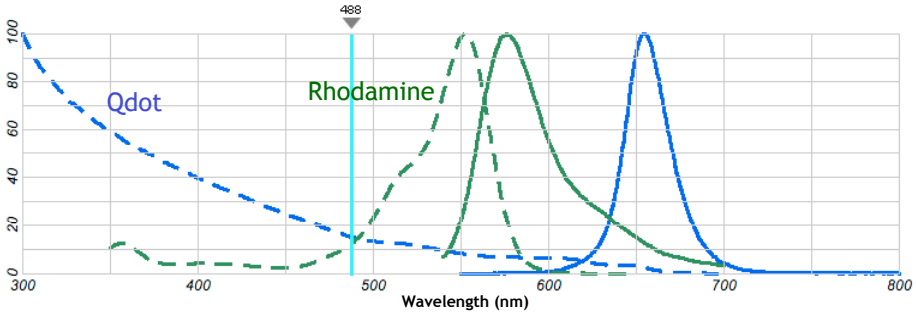

b

Figure 6: Quantum Dots (QDs) as fluorescent probes. (a) Electron micrograph of a QD (left). The QD is capped with a passivating shell, coated with polymer, and conjugated to a bioactive molecule (here streptavidin) as schematically depicted on the right-hand side. **(b)** Comparison of the excitation spectra (dotted lines) and emission spectra (full lines) of a QD 655 (blue) and Rhodamine (green). Graph retrieved from http://probes.invitrogen.com/resources/spectraviewer/.

3 Results and Discussion

In this chapter the experimental results concerning the implementation, characterization, and application of 3-D interference-based nanometer tracking are presented.

First of all, a general investigation of 3-D interference-based nanometer tracking was performed to explore the potential of the method in various settings. The next step was to probe microtubule structure. In particular, the supertwist pitches of microtubule preparations with known structural characteristics were measured using the microtubule plus-end-directed motor kinesin-1, which is known to follow the protofilament axis of microtubules. This way, the applicability of the 3-D tracking method in the setup of a nanotransport related gliding motility assay was proven. In addition, the effect of manipulating the microtubule surface by subtilisin treatment on the path of kinesin-1 was investigated. Still using the processive kinesin-1 motor in the gliding geometry, the impact of large cargo on the rotation and forward movement of microtubules as nanoshuttles was analyzed. Finally, the capability to generate torque was studied for two potential counter-players of kinesin-1 in nanotransport systems, namely the microtubule minus-end-directed motors 22S dynein and ncd.

The results are discussed in relation to earlier studies and regarding their implications for nanotransport based on biomolecular motors.

Major parts of the results, specifically of those presented in Chapters 3.1 to 3.5 have been published [106].

3.1 Characterizing Interference-Assisted 3-D Tracking

To determine the capabilities and the limits of interference-based 3-D tracking (see Chapter 2.4) red-emitting QDs (emission wavelength 655 nm) and yellow-green–fluorescent FluoSpheres beads (40 nm diameter, Molecular Probes) were unspecifically bound to the surface of silicon chips with a 30 nm thermal oxide layer. This is the same thickness of oxide, which has later been used with the gliding motility assays. Therefore, the position of the surface-bound QDs here corresponds approximately to the minimum possible height (and thus the lowest fluorescence signal due to FLIC) of the QDs in experiments where the rotation of the microtubules was intended to be characterized. Because the precision is strongly determined by the number of detected photons, the values derived here present worst case scenarios, i.e. lower bounds for the accuracy.

To explore the full potential of 3-D tracking based on FLIC microscopy, not only the typical imaging settings used for the characterization of microtubule rotation were looked at. Rather, the following settings were additionally tested: (i) QDs vs. fluorescent beads; (ii) arc lamp illumination vs. high power laser illumination; (iii) slow vs. fast time resolution (Figure 7). More photons were obtained and thus better localization was achieved using the fluorescent beads, high power laser illumination and lower image acquisition rates. Inversely, localization was worse when QDs, arc lamp illumination, and higher frame rates were used. The data were then analyzed and localizaton precision was estimated in *xy*-direction and in *z*-direction separately.

Conditions	Data	Accuracy
QD 655 with arc lamp at 10 fps	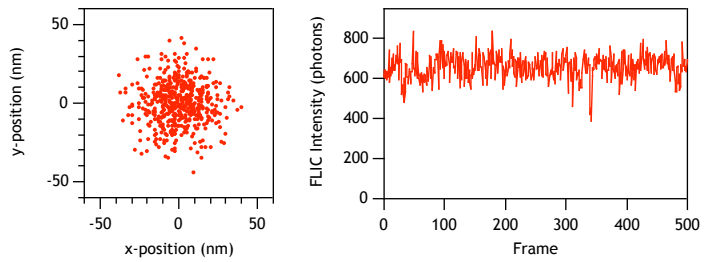	x: 13.6 nm y: 13.7 nm
QD 655 with laser at 10 fps	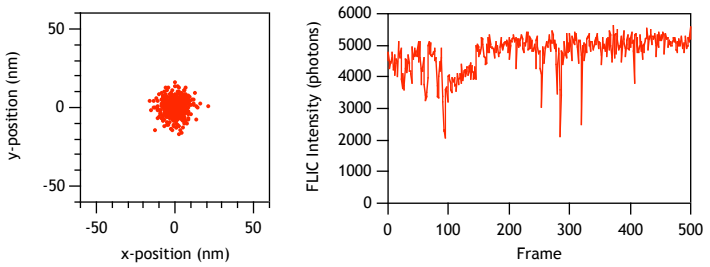	x: 5.1 nm y: 5.3 nm
QD 655 with laser at 100 fps	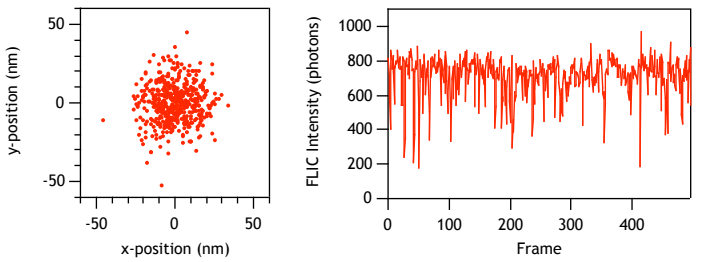	x: 11.5 nm y: 12.3 nm
Bead with laser at 100 fps	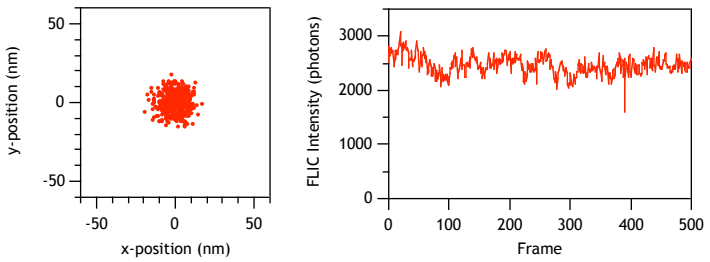	x: 6.0 nm y: 6.1 nm

Figure 7: Noise from imaging and impact on localisation. Nanometer tracking results for red QDs and yellow-green fluorescent beads immobilized on silicon chips with a 30 nm thermal oxide layer. Imaging in FLIC-mode was performed with frame rates of 10 and 100 fps using arc lamp or laser illumination.

The precision, by which the QDs could be localized in *xy*-direction, was determined as the standard deviation of the tracked positions (Figure 7). All data acquired with 10 frames per second (fps) were drift-corrected using the average position of up to 5 other stationary objects as reference points

[95]. Using arc lamp illumination in conjunction with imaging at 10 fps a precision of about 14 nm in *xy*-direction was determined. When laser illumination was utilized, this value improved (accuracy of about 5 nm at 10 fps) or data acquisition could be performed at higher frame rates (100 fps with an accuracy of about 12 nm at for QDs and 6 nm for fluorescent beads). For comparison, the amplitude of the expected sideways excursions of QDs attached to rotating microtubules are estimated to be in the order of 50 nm. That is the 25 nm diameter of microtubules plus a distance of 10 to 15 nm between microtubule surface and center of the QD. Thus the deduced localization values are sufficient to observe rotations of microtubules.

The accuracy of the measured *z*-position in FLIC-based imaging, is directly affected by any noise in the detected fluorescence emission. Figure 7, first row, represents a setting which was used for the majority of experiments that will be dealt with later in this work. Under these conditions the standard deviation in the FLIC intensity was about 9 % of the averaged intensity. Assuming that the intensity of the QD on top of the 30 nm silicon oxide layer is less than half of the intensity expected in the first FLIC maximum (which typically occurs at about a quarter of the wavelength, i.e. at about 125 nm above the reflective silicon / silicon oxide interface in water), the measured fluctuations corresponded to less than 4.5 % of the maximum intensity. Although the exact shape of the FLIC-curve has not been determined in this study, roughly a slope of one (i.e. 100 % intensity change over 125 nm height change) might be assumed. A value of 4.5 % intensity variation would then translate into ~6 nm accuracy in the *z*-direction. It has to be noted that this is a very rough estimate, which will depend critically on further parameters, such as the blinking of each individual QD.

The analyzed data might also indicate that larger intensity fluctuations arise under stronger QD excitation (Figure 7, row 2, standard deviation = 12 %) and higher data acquisition rates (Figure 7, row 3, standard deviation = 18 %). The latter shows that faster imaging avoids averaging over some of the dark-states that occur during blinking at timescales below 100ms. In contrast, imaging of a fluorescent bead showed less noise (Figure 7, row 4,

standard deviation = 7 %) and demonstrates the possibility to improve the method when turning to non-blinking probes. However, it is not suggested that individual QDs have been used to determine absolute height values here. Rather, the purpose is to prove that experimental noise is sufficiently low to detect relative height changes that are derived from QD fluorescence intensity signals as they are moved up and down. This is definitely the case for estimated amplitudes of approximately 50 nm as they would occur for QDs that are attached to gliding and rotating microtubules.

As with other single particle tracking methods, the maximum speed of imaging is given by the maximum rate of image acquisition of the employed camera. In the case of electron-multiplied CCD cameras, frame rates of subregion readout are possible up to about 1000 fps. However, the tracking accuracy is limited by the number of detected photons (and the signal-to-noise ratio), which logically decreases with shorter exposure times. One appropriate means to then increase the photon number again is to use brighter probes, which can for example be achieved by clustering of QDs [98]. However, with the current generation of CCD cameras even then a frame rate beyond 100 fps would practically be impossible for imaging of objects moving over longer distances. Since full frame imaging is comparably slow, even at image acquisition rates of 100 fps, only a subsection of the CCD chip can be used to record images. The resulting reduced field of view means firstly a lower number of observable events and secondly shorter distances during which the behavior of microtubules can be followed.

What do the feasible imaging rates of up to 100 fps mean for the detection of microtubule rotations? Assuming typical parameters of a kinesin-1 gliding motility assay at room temperature and saturating ATP concentration, microtubule velocity would be ~1 µm/s. At an image acquisition rate of 10 or 100 fps this corresponds to 10 or 100 data points respectively per full rotation if the rotational pitch was 1 µm. This has turned out to be sufficient in the case of the experiments that were conducted for this work. However, it also shows that if movement is much faster than 1 µm/s or the rotational pitch much shorter than 1 µm, the

available temporal resolution needs to be checked, whether it is still sufficient.

The FLIC-based method provides similar sensitivity as state-of-the-art 3-D tracking based on dual-focus imaging [98, 99]. Regarding some specific features the interference-based 3-D tracking offers additional advantages:

1. It is very easy to implement in terms of instrumentation and can be used with any standard fluorescence microscope where illumination is achieved by either arc lamp or laser.
2. The height data can directly be visualized by a maximum projection over time or time-space-plots (kymographs). This way immediate semi-quantitative analysis of height changes of a probe becomes possible.

When further optimized, it additionally offers the potential to retrieve absolute height values above the substrate surface [101]. While the accuracy of the interference-based 3-D tracking method is currently limited by blinking in the QD emission, most likely the approach will strongly benefit from future research to further improve the optical properties of QDs [105] or other fluorescent markers [107].

In conclusion, the interference-based 3-D tracking has been found to meet the requirements in both spatial precision and temporal resolution to detect microtubule rotation in typical gliding motility assays. That being said, it can be expected that the development of faster cameras and brighter, non-blinking fluorophores will even further increase the power of this technique.

3.2 Measuring Microtubule Supertwist Pitches Using Kinesin-1

Knowing that the 3-D nanometer tracking approach is in principle capable of providing sufficient resolution to follow the motion of microtubules in 3-D, the next step was to test whether it can really be used to detect the rotation of microtubules in gliding motility assays precisely and reliably. An ideal test system would be one where the pitch and direction of rotation of the microtubules is already known. This is the case for a gliding assay where

kinesin-1 propels microtubules that are self-assembled under defined conditions. It is known for kinesin-1 that it follows the axis of single microtubule protofilaments [5, 17]. Moreover, it is known from electron microscopy studies that certain assembly conditions favor the growth of microtubules comprising a specific number of protofilaments [17, 26, 27]. As described in Chapter 2.1, the structure of the microtubule surface is closely related to the number of protofilaments. Microtubules with 13 protofilaments exhibit no supertwist. In contrast, it has been reported that about 95 % of the microtubules grown in the presence of GMP-CPP are composed of 14 protofilaments [26, 108] - leading to a characteristic left-handed supertwist with a pitch between 7.75 ± 0.33 µm [J. Howard, personal communication] and 8.95 ± 1.36 µm [108]. A procedure to induce the self-assembly of microtubules with consistently 12 protofilaments is not known. However, the presence of taxol during self-assembly has been found to favor 12 protofilament microtubules [17, 26, 109-111]. Performing electron microscopy on this type of microtubules has revealed a right-handed supertwist with a pitch between ~3.5 µm and ~4.5 µm [17, 108, 110]. In combination this means that kinesin-1 follows the routes that are indicated in Figure 8. In a kinesin-1 gliding assay this translates to a microtubule rotation with a pitch according to the supertwist.

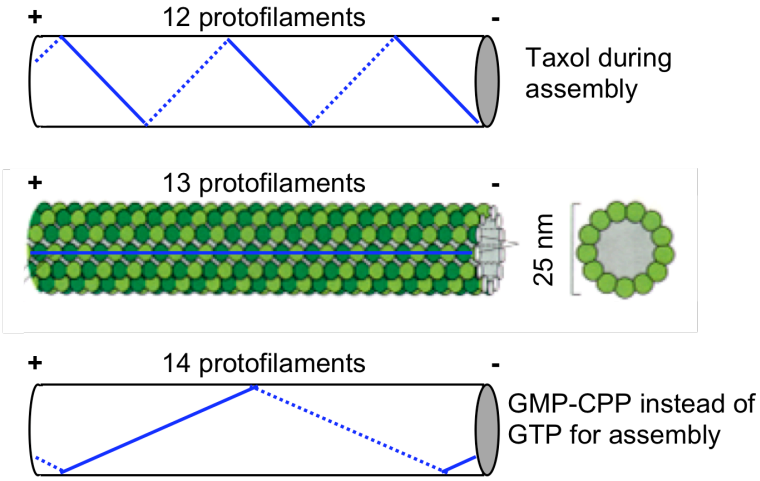

Figure 8: Protofilament arrangement for microtubules grown under different assembly conditions. The presence of taxol during growth favors microtubules comprising 12 protofilaments. These exhibit a right-handed supertwist. Microtubules with 13

protofilaments as they usually occur *in vivo* have straight protofilaments. When growing microtubules in the presence of GMP-CPP they are almost exclusively composed of 14 protofilaments and exhibit a left-handed supertwist.

To test whether microtubule rotation can be measured in agreement with the expected supertwist values, reconstituted GMP-CPP microtubules were sparsely labeled with QDs [87, 112]. Fluorescence microscopy with arc lamp illumination was used to image their longitudinal and rotational movement over reflective silicon surfaces, which were coated with dimeric kinesin-1 motor proteins (Figure 9). In order to achieve better signal-to-noise ratios, the used silicon surfaces were primed with a thermal oxide layer of approximately 30 nm. The 2-D *xy*-positions of the QDs were determined with sub-pixel accuracy using nanometer tracking (Chapter 2.3). These data were then combined with simultaneous height measurements based on FLIC microscopy. As pointed out in Chapter 2.4, FLIC leads to a periodic modulation of the detected emission intensity as a function of height above the surface. Minimum intensity is observed directly on the surface, while the first maximum is located about 100-150 nm above the reflective interface. Thus, QDs (diameter of about 20 nm) attached to rotating microtubules (diameter of 25 nm) gliding at an average height of about 30 nm [101] are expected to periodically change their emission intensity as they are moved up and down. Given that the QDs will stay below the height of the first maximum, minimum FLIC intensity occurs when the QD is closest to the surface (that is when the QD is located between the microtubule and the surface), while maximum FLIC intensity corresponds to the QD position farthest away from the surface.

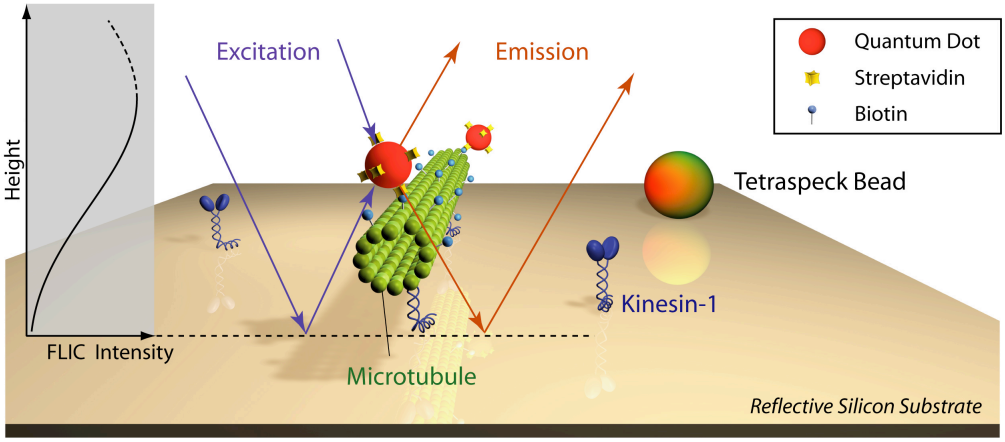

Figure 9: Scheme of gliding motility assay to measure microtubule rotation. Optical dual-color 3-D nano-imaging is performed in an *in vitro* gliding motility assay on a reflective silicon substrate. QDs (red emission) are attached to motor-propelled microtubules (labeled by Alexa488, green) via biotin-streptavidin linkage. Imaging is performed using dual-color fluorescence microscopy, where a dichromatic beamsplitter between the microscope and the camera separates the red and green signals onto different parts of the CCD camera chip. Due to FLIC, the recorded fluorescence intensities increase as function of distance above the substrate surface. In order to avoid very low fluorescence intensities of objects located in close proximity to the reflective silicon substrate, surfaces were primed with a ~30 nm transparent silicon oxide layer (not shown in the picture). Multi-fluorescent tetraspeck beads were used for spatial alignment when superimposing the images from the different color channels.

A periodic intensity variation along the path of the microtubule became directly visible in a maximum projection of the QD signals over time (Figure 10a). Quantitative fluorescence data as function of distance traveled by the microtubules were obtained by tracking the intensity values and the *xy*-positions of the QDs for each frame of the recorded time series (Figure 10b). For statistical treatment, the transport of 146 QDs (on 98 microtubules) was investigated. 41 of the QD traces were rejected because the traces were shorter than 15 µm (about twice the length of the expected supertwist for a microtubule with 14 protofilaments), the overall QD signal was too low, or a perturbing event like microtubule crossing occurred. The remaining events were then categorized into the following classes: 94 % rotating (showing at least two clear maxima or minima), 5 % non-rotating and 1 % 'unclear' (i.e.

non-classifiable) events. Plotting the periodicities of the rotation events into a histogram (Figure 10c) revealed a main peak with an average periodicity of 7.86 ± 1.37 µm (mean ± standard deviation, n = 99).

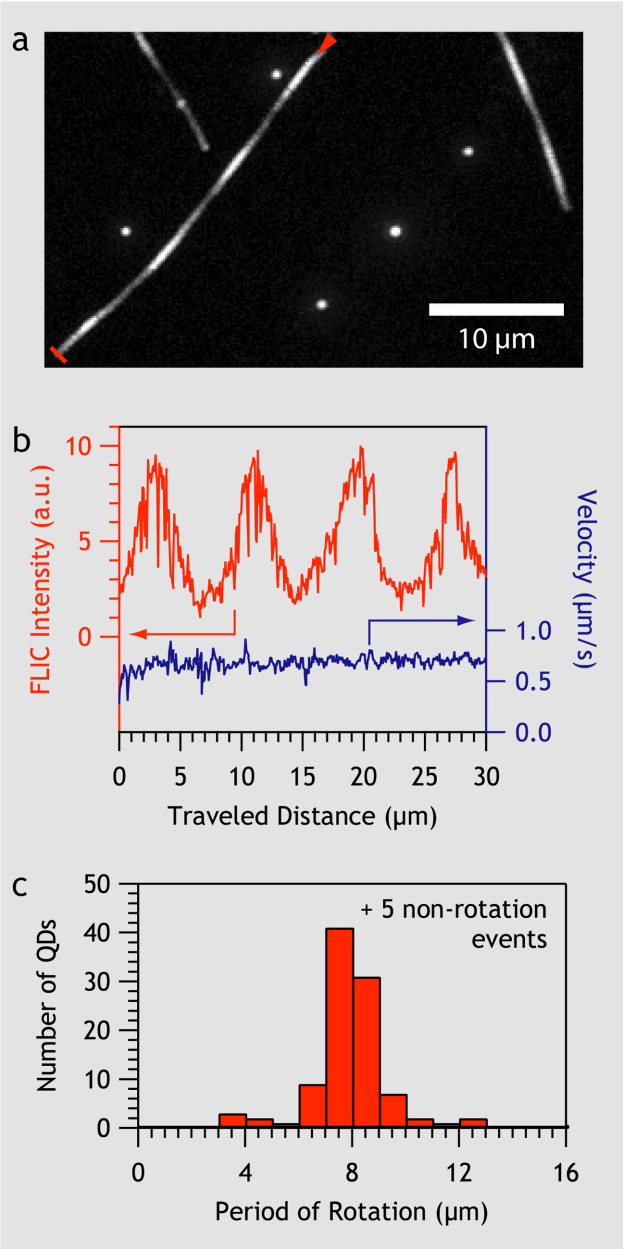

Figure 10: Rotation of GMP-CPP microtubules. FLIC microscopy of QDs attached to gliding microtubules (self-assembled in the presence of GMP-CPP) driven by kinesin-1. Imaging was performed at a rate of 10 fps using arc lamp excitation. **(a)** Characteristic maximum projection of recorded QD signals over time. **(b)** Typical intensity (red) and velocity (blue) traces vs. traveled distance for a microtubule-attached QD. Data correspond to the marked maximum projection in (a). **(c)** Histogram of measured rotational periodicities on kinesin-1-coated surfaces (periodicity = 7.86 ± 1.37 µm, mean ± standard deviation, n = 99).

To ensure that the assembly of microtubules in the presence of rhodamine-labeled and biotinylated tubulin did not alter the fine-structure of the grown filaments, GMP-CPP microtubules were also grown from purely unlabeled tubulin as a control. Biotinylation was performed on assembled microtubules. Microtubules prepared in this way displayed similar behavior in kinesin-1 gliding assays (periodicity = 7.99 ± 1.01 µm, mean ± standard deviation, n = 21 microtubules) as those assembled from pre-labeled tubulin.

The obtained average periodicities fit previously reported supertwist pitches for GMP-CPP microtubules with 14 protofilaments very well (see above). Therefore, it can be assumed that the periodic FLIC intensity curves provide a suitable means to detect the rotation of gliding microtubules.

To exclude the possibility that the detection of rotation of GMP-CPP microtubules was an artifact and to verify that no periodic FLIC signal occurs in the absence of a supertwist, further microtubule preparations were tested for their behavior in kinesin-1 gliding assays. Other microtubule assembly conditions are known to lead to more heterogeneous but characteristic distributions of protofilament numbers. Consequently, microtubule preparations that, according to previous electron microscopy studies, are characterized by increased percentages of microtubules composed of 12 and 13 protofilaments [17, 108, 109] were chosen for the additional experiments. Detailed protocols of the assembly conditions can be found in Chapter 5.1.

Kinesin-1 gliding assays were performed as for the GMP-CPP microtubules and analyzed in the same way. The statistics of the measurements are given in Table 1 along with histograms of the rotational periods and typical sample traces in Figure 11.

Preparation Method	Total QDs (MTs)	Investiga-ted QDs	Rotating	Non-rotating	Unclear
BRB80 + Taxol	78 (48)	46	63 %	20 %	17 %
BRB80	77 (68)	63	68 %	19 %	13 %
MES + DMSO	77 (70)	64	41 %	37 %	22 %

Table 1: Classification of various gliding microtubule populations and attached QDs. Statistical analysis of the total number of QDs transported by the total number of microtubules (MTs) prepared by different methods in the presence of GTP. A number of transport events were rejected because the FLIC intensity traces were shorter than 15 µm (about twice the length of the expected supertwist for a microtubule with 14 protofilaments), the overall QD signal was too low, or a perturbing event (such as microtubules crossing each other) occurred. The remaining 'investigated' QD transport events were classified into rotating (showing at least two clear maxima or minima), non-rotating and unclear events.

Method	Period Histogram	Typical Sample Traces
BRB80 + taxol	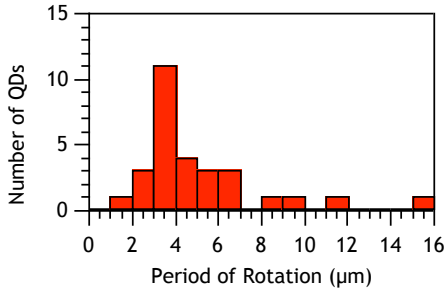	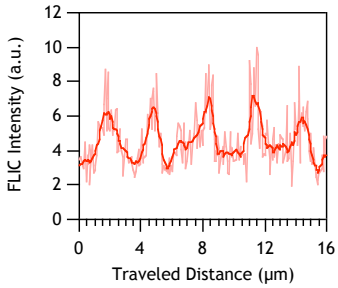
BRB80	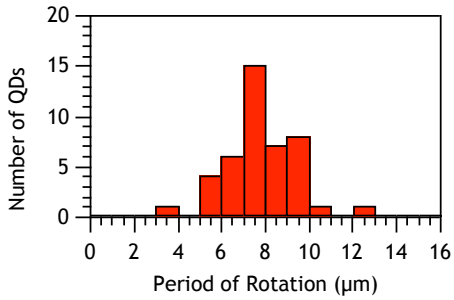	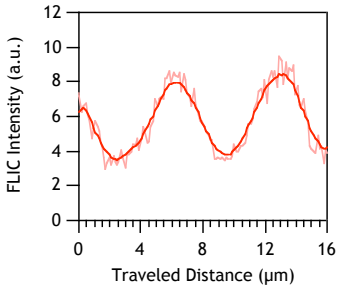
MES + DMSO	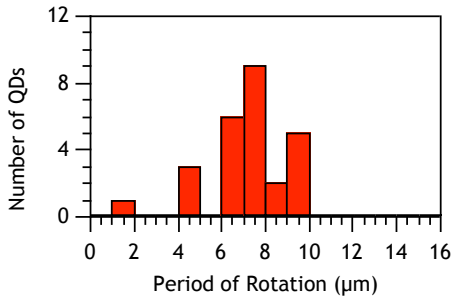	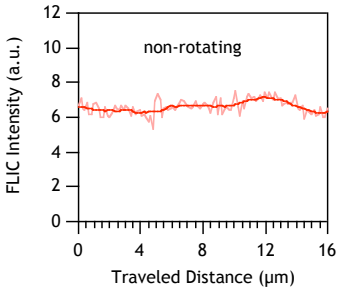

Figure 11: Analysis of the investigated QD transport events on differently prepared microtubules. Histograms of the rotational periodicities identified in the populations of rotating microtubules (middle column). Typical FLIC intensity traces for the given microtubule preparations (right column).

The obtained data on the microtubule rotations correspond well to published results of microtubule structures based on electron microscopy:

1. Microtubules grown in the presence of taxol and GTP were shown to be mainly (77 %) composed of 12 protofilaments with a predicted supertwist pitch of about 3.4 µm [17]. The BRB80 + taxol microtubule data here reproduce these findings, including a significant number of non-rotating microtubules, presumably consisting of 13 protofilaments (11 % in ref. [17]).

2. Microtubules grown in BRB80 without dimethyl-sulfoxide (DMSO) or glycerol were shown to be mainly (49 % in ref. [108] or 61 % in ref. [17]) composed of 14 protofilaments with a supertwist pitch that was significantly shorter than that of 14 protofilament microtubules grown in the presence of GMP-CPP [108]. The BRB80 microtubule data here reproduce these findings, including a number of non-rotating microtubules presumably consisting of 13 protofilaments (38 % in ref. [108] and 32 % in ref. [17]). It has to be noted that a recent electron microscopy study [113] differs notably from these data. About 75 % of microtubules assembled under comparable conditions were reported to consist of 13 protofilaments. The reason for this difference is unclear, but could be due to the specific tubulin preparation used.
3. Microtubules grown in MES and DMSO were shown to contain a large number (54 % in ref. [17]) of non-rotating microtubules composed of 13 protofilaments. The MES + DMSO microtubule data here reproduce this finding, including a significant number of microtubules consisting of 14 protofilaments (38 % in ref. [17]). Note, that in the gliding motility experiments conducted here a number of the unclear events might in fact correspond to the class of 'non-rotating' 13 protofilament microtubules that still can exhibit long-pitched supertwists with lengths down to 25 µm [17]. For the reliable detection of such long periodicities, the observed microtubule traces were in general too short. Furthermore, it cannot be completely excluded that microtubules and attached QDs get lifted up on the surface due to invisible obstacles, which could be mistaken for a rotation. However, there is no indication that this occurs to a relevant degree.

Given the good agreement of the presented measurements with previous electron microscopy studies, interference-based 3-D tracking is suggested to provide an attractive and easy-to-use alternative to study the fine structure of cytoskeletal filaments.

3.3 Determining Microtubule Supertwist Handedness

While FLIC-microscopy on its own is a convenient tool to determine the periodicities of microtubule rotations, it does not provide sufficient information to determine the handedness of rotation. However, if the sideways excursion of the QD with respect to the microtubule centerline is known, the complete 3-D trajectory of the QD with respect to the microtubule can be reconstructed. Furthermore, this additional piece of information provides the rotational pitch and can therefore serve as a cross check for the pitch that is derived from the FLIC intensity signal. To obtain the according data, simultaneous dual-color FLIC imaging (Figure 12a) was performed and the *xy*-positions of the microtubules (emitting in the green) were tracked in addition to the QD positions (emitting in the red). Finally, the sideways deviations of the QDs from the microtubules were calculated for each frame of the recorded time series. The resulting sinusoidal curves exhibited the same periodicities as the FLIC intensity curves (Figure 12b, c).

For GMP-CPP microtubules (Figure 12b), zero QD sideways deviation occurred at a peak of the FLIC intensity curve (state 1). Upon movement of the microtubule this was followed by the maximum sideways deviation to the left at an intermediate FLIC intensity (state 2). Thereafter, zero sideways deviation at a minimum of the FLIC intensity curve (state 3) occured before the maximum sideways deviation to the right at an intermediate FLIC intensity (state 4). The geometrical arrangement (inset in Figure 12b) of these states corresponds to a counterclockwise rotation of the microtubule when looking in the direction of motion. An example of clockwise rotation is given in Figure 12c. The analyzed microtubule was grown in the presence of GTP and taxol, a condition under which 12 protofilament microtubules are preferably formed (see above). The counterclockwise and clockwise rotations result from the different structural orientations in the supertwist of microtubules comprising 14 and 12 protofilaments, respectively [114].

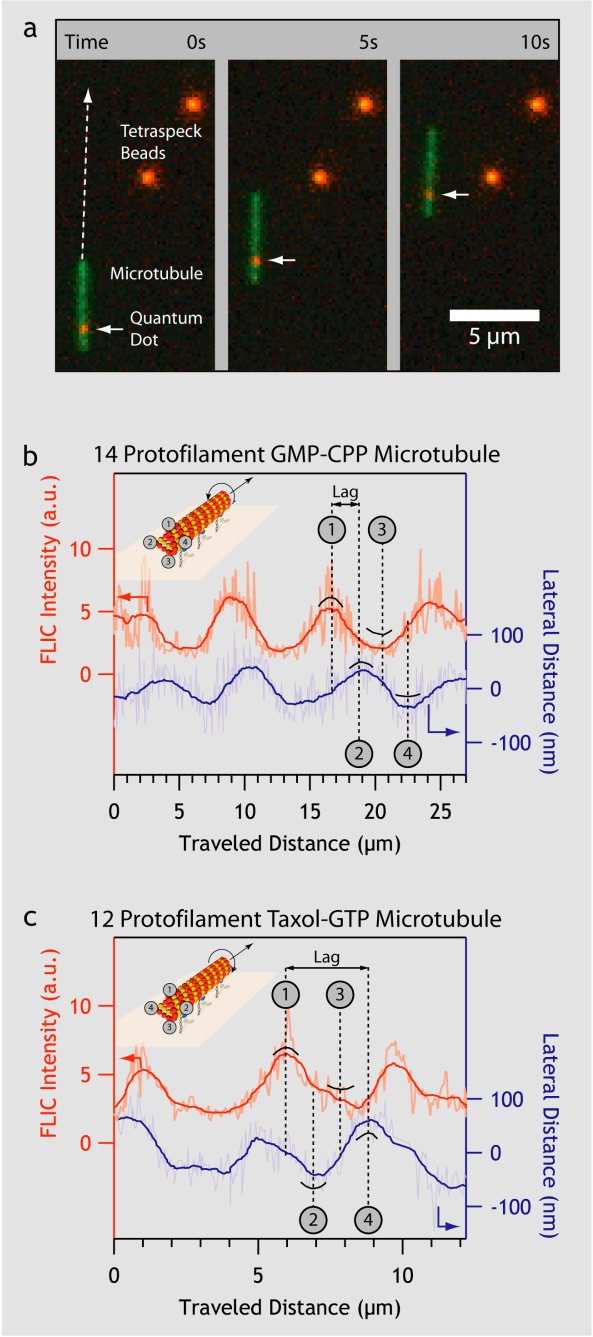

Figure 12: Determining of the direction of rotation using dual-color FLIC-imaging. (a) Color-overlaid time series of motile microtubule (green) with attached QD (red) simultaneously recorded on the two halves of the CCD camera chip (image acquisition rate of 10 fps). **(b)** XY-deviation of QD from microtubule (lateral distance) and FLIC intensity vs. traveled distance for a 14-protofilament GMP-CPP microtubule (typical rotational period about 8 µm). The inset illustrates counterclockwise rotation (looking in the direction of motion) derived from the temporal sequence of the 3-D QD positions relative to the microtubule. **(c)** Clockwise rotation of a 12-protofilament microtubule (typical rotational period about 4 µm) assembled in the presence of GTP and taxol [108, 109, 114].

To assure that the shift between *xy*-tracking data and the FLIC intensity curve was also quantitatively correct, circular cross-correlation between both signals was performed (Figure 13). In case of the GMP-CPP microtubules the measured phase shift of 1.8 µm (approximately one quarter of the full period length) indicated counterclockwise rotation. In contrast, for the taxol-GTP microtubule the phase shift was in the order of three quarters of a full period length, indicating a clockwise rotation of the microtubule.

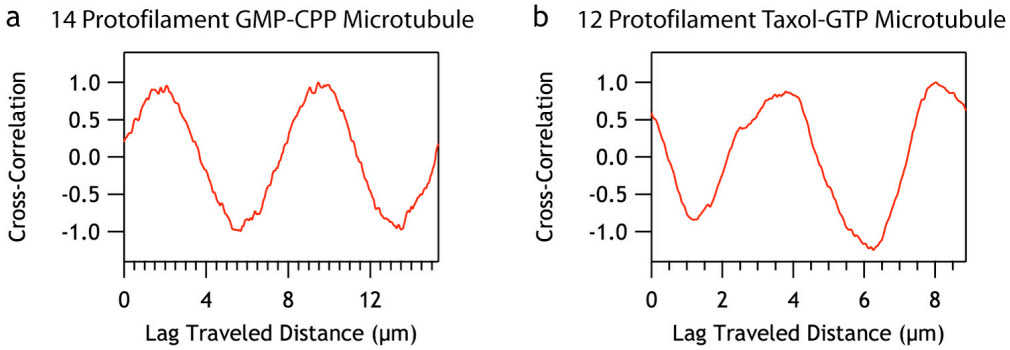

Figure 13: Correlation and phase shift between FLIC signal and *xy*-data. Cross-correlation between FLIC intensity and lateral distance vs. the lag of traveled distance. The cross-correlations in **(a)** and **(b)** are derived from the data in Figure 12b and c, respectively. For this analysis, two full periods (based on the FLIC signals) were excised from the original data, because otherwise severe edge effects can arise when cross-correlating signals of short length. In case of the 14 protofilament GMP-CPP microtubule, the distance between the two peaks of the cross-correlation function was about 7.8 µm and corresponded to the periodicity of rotation. The position of the first peak of the cross-correlation function indicates the lag (phase shift) of the sideways deviation curve with respect to the FLIC intensity curve.

Combining the information of both FLIC intensity curves and *xy*-tracking data, consistent values for the rotational pitch of gliding microtubules were obtained. In addition, it was possible to reconstruct the QD positions with respect to the moving microtubule in 3-D space and to directly deduce the orientation of microtubule rotation. The obtained values were consistent with the corresponding supertwists.

3.4 Rotation of Subtilisin-Treated Microtubules

A remarkable property of kinesin-1 is that it can identify the axes of microtubule protofilaments with high fidelity [5, 17]. However, it is not known whether and to which extend this capability can be tuned or disturbed by modifications of the microtubule lattice. Also, it is not known how modifications of the microtubule surface might influence the paths that other motor proteins are choosing on the microtubule lattice.

An interesting example in this respect is the interaction of kinesin-1 with the so-called E-hook. The E-hook is the flexible, glutamate-rich and therefore highly negatively charged C-terminus of tubulin that is exposed on the microtubule lattice. It has been shown that the E-hook interacts with kinesin-1 conferring increased speed and processivity to the motor protein [115, 116]. An electrostatic interaction between the negatively charged E-hook and the positively charged neck region of kinesin-1 [115, 116] or alternatively an interaction of the E-hook with the kinesin-1 heads [117] have been proposed as the molecular basis. In particular, it has been shown that specific removal of the E-hook by subtilisin digestion [118, 119] results in a decreased run length of kinesin-1-coated beads in *in vitro* bead assays. Furthermore, reduced velocities of motility have been reported when using subtilisin-digested microtubules in kinesin-1 stepping assays [115-117] and kinesin-1 gliding motility assays [101, 117].

The question, whether the tubulin E-hook is required for kinesin-1 to track the protofilament axis of a microtubule, was addressed by removing E-hooks from GMP-CPP microtubules and subsequently studying their rotation during gliding on a kinesin-1-coated surface.

E-hooks were removed by subtilisin treatment of the assembled microtubules. Successful digestion of E-hooks was verified by sodium dodecyl sulfate polyacrylamide gel electrophoresis (SDS-PAGE; Figure 14). Moreover, successful subtilisin treatment was confirmed by characterization of microtubule velocities in gliding motility assays with kinesin-1. For undigested control microtubules (that were exposed to the identical digestion procedure, only without subtilisin) an average velocity of 0.78 ±

0.04 µm/s (mean ± standard deviation, n = 10) was determined, while for digested ones this value was 0.57 ± 0.10 µm/s (mean ± standard deviation, n = 11). This is in very good agreement with previous reports from other groups (see above).

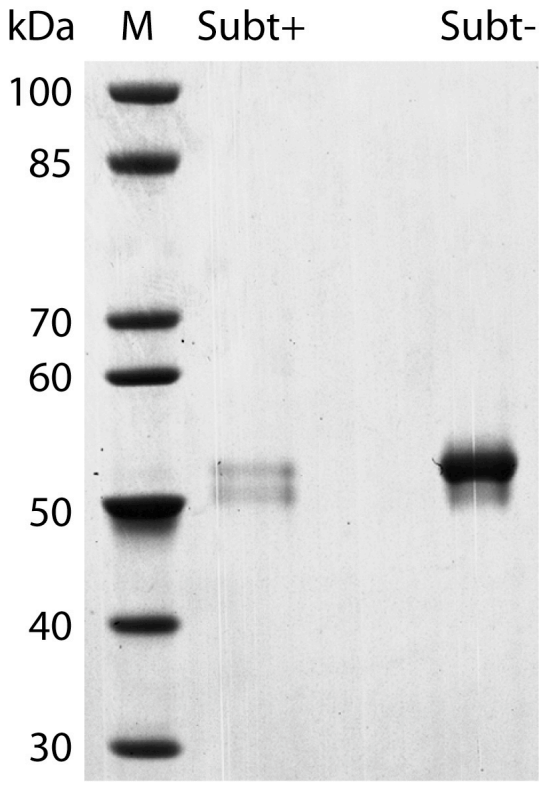

Figure 14: SDS-PAGE for verification of E-hook cleavage. 'M' denotes the Marker, 'Subt+' the subtilisin-digested microtubules, and 'Subt-' the non-digested control microtubules (note that the Subt- microtubules were taken through the identical digestion procedure as the Subt+ microtubules – only without subtilisin).

To characterize rotations of subtilisin-treated microtubules in kinesin-1 gliding motility assays, the same experimental setup as before (Figure 9) was used where QDs attached to moving GMP-CPP microtubules were imaged on a reflecting surface. Applying 3-D tracking analysis, the rotational pitches stemming from 12 subtilisin-treated and 15 undigested control microtubules were plotted into histograms (Figure 15).

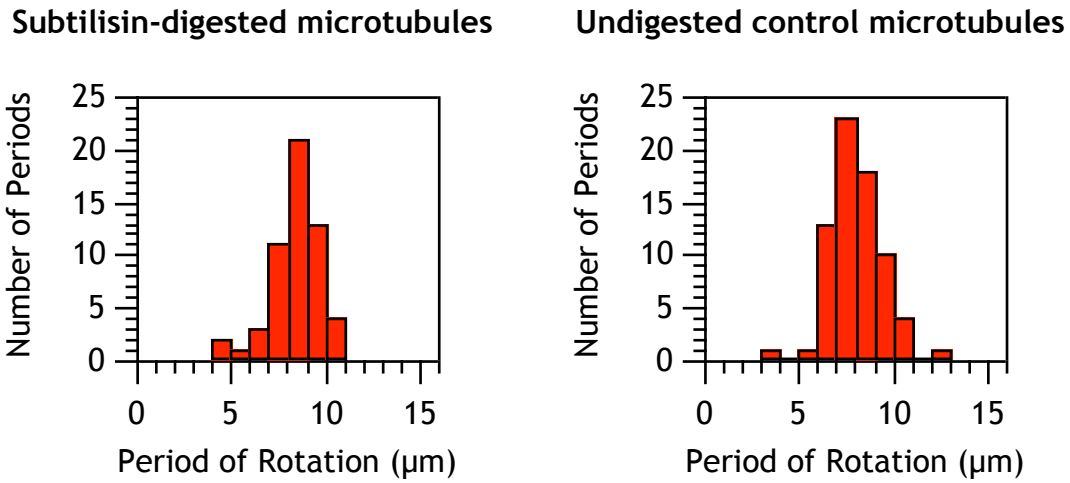

Figure 15: Effect of E-hook cleavage on gliding motility with kinesin-1. Rotational pitches for microtubules (self-assembled in the presence of GMP-CPP) were derived from FLIC microscopy of QDs that were attached to gliding microtubules driven by kinesin-1. **(a)** Subtilisin-treated microtubules were rotating with a periodicity of 8.37 ± 0.17 µm (mean ± SEM, total number of detected periods = 55, from 12 microtubules). **(b)** Undigested control microtubules displayed a periodicity of 7.98 ± 0.16 µm (mean ± SEM, total number of detected periods = 71, from 15 microtubules).

Analyzing the data of subtilisin-treated microtubules revealed an average periodicity of 8.37 ± 0.17 µm (mean ± SEM, total number of detected periods = 55). In control measurements, undigested GMP-CPP microtubules displayed a periodicity of 7.98 ± 0.16 µm (mean ± SEM, total number of detected periods = 71). Performing a t-test on these data a t-value of 1.65 was obtained. Thus, there is no evidence (at 95 % confidence level) that kinesin-1 requires the interaction with the tubulin E-hook in order to track the microtubule protofilament axis.

In spite of the negative result the example presented here provides a proof-of-principle on how to test the impact of microtubule modifications on the path that motor proteins follow on the microtubule lattice. Firstly, any other microtubule motor than kinesin-1 could be investigated. Secondly, instead of cleaving the tubulin E-hook, alternative modifications of the microtubule lattice might be of interest. One possibility might be to alter or remove structural features of microtubules that are specifically recognized

by motor proteins. The purpose could be a modification or stabilization of the rotation behavior of microtubules used as nanoshuttles in gliding motility assays. Furthermore, different kinds of microtubule binding partners, e.g. MAPs, antibodies, aptamers or other, artificial cargo could be imagined to affect trajectories of motor proteins on the microtubule lattice.

3.5 Transport of Large Cargo by Gliding Microtubules

So far, it has been shown that supertwisted microtubules acting as nanoshuttles do rotate very robustly around their longitudinal axis on kinesin-1-coated surfaces. It has further been demonstrated that small cargo, which is represented by QDs, does not cause detrimental effects on the motion of the nanoshuttles. The situation is completely different for large cargo in the mircrometer-range. In this case, the microtubule-attached objects do not fit between the microtubule and the surface. This potentially poses a serious problem because it may be expected that cargo is pushed against the surface in the direction of microtubule rotation. Possible consequences are that cargo is stripped off its transporter if it is not sufficiently strongly bound or that the sideways drag perturbs the motion of the nanoshuttle. Since kinesin-1 follows the microtubule protofilament axis, the use of microtubules with 13 protofilaments might alternatively be suggested to avoid supertwist and resulting rotation. However, it has to be remarked that the production of microtubules with exclusively 13 protofilaments but without lattice defects is not trivial. Moreover, even for microtubules with presumably 13 protofilaments, long-pitched supertwists (> 25 µm) have been reported [17]. Therefore, nanotransport with microtubule shuttles will always be accompanied by filament rotation.

Consequently, interference-based 3-D tracking was used to investigate what happens to the rotational movement of gliding microtubules during the pick-up of 'large' cargo (Figure 16). The rotations of 'unladen' GMP-CPP microtubules were detected by QD-assisted FLIC measurements and changes of the rotational behavior were observed in situ when the microtubules

picked up 2.8 µm beads from the solution, the substrate surface or other microtubules (Figure 16a). Rotation of microtubules could be verified in kymographs directly (Figure 16b) or by analyzing *xy*-tracking data in combination with FLIC intensity values of the transported QD (Figure 16c). Once being loaded onto the microtubules, most of the beads were transported over distances longer than the observation area. Stable attachment of the beads to microtubules can be assured by checking that the distance between bead and QD remains constant (Figure 16b) and the position of both objects does not change with respect to the microtubule ends. Rotation of microtubules was stopping upon cargo pick-up. This can be concluded from the fact that rotation of the (dimly fluorescently labeled and therefore visible) microtubules with stably bound 2.8 µm beads would have been directly visible in the fluorescence movie of that event. Coinciding with the cargo pick-up, periodic changes of the FLIC intensity signal from the QDs disappeared (Figure 16b, c), providing additional prove that microtubule rotation stopped. When a bead-carrying microtubule dropped off its cargo, it showed the inverse behavior of a microtubule during cargo loading and resumed its rotational motion (Figure 16d-f).

Interestingly, the forward speed of the gliding microtubules was only minimally impacted when microtubule rotation stopped upon cargo pick-up (Figure 16c). The speed before cargo pick-up was 676 ± 14 nm/s (mean ± standard deviation, n = 13 microtubules). For any out of these 13 microtubules, a slight slow-down was measured when cargo pick-up occurred and was determined to be 4.1 ± 2.0 % (mean ± standard deviation).

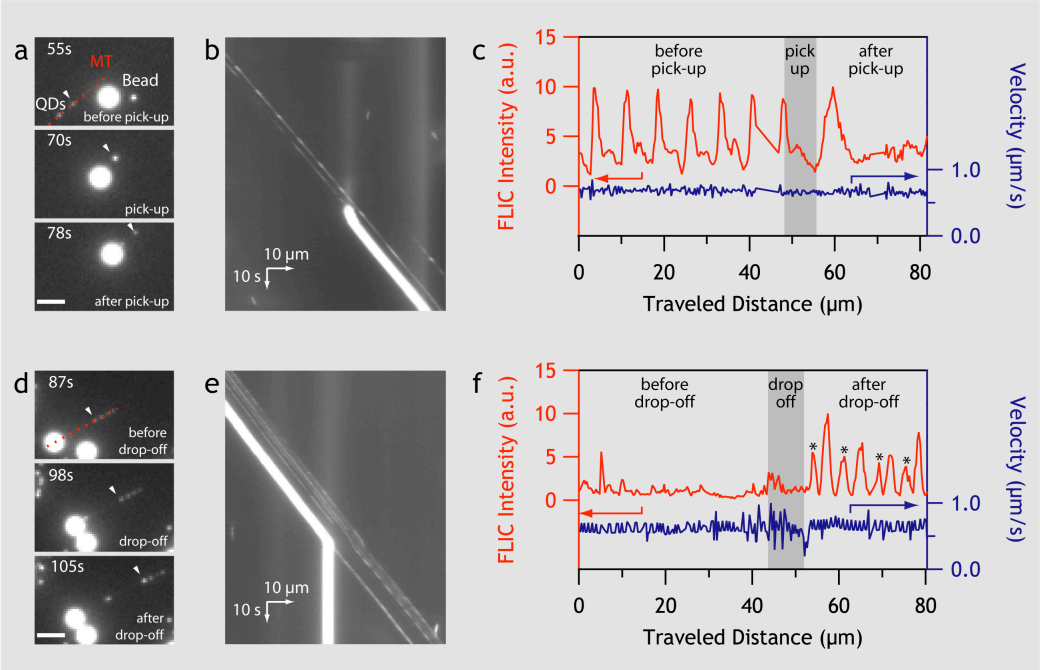

Figure 16: Microtubule rotations during pick-up and drop-off of micron-sized cargo. (a) Fluorescent images of a motile microtubule (MT, red dotted line) with two QDs (small dot-like signals) picking up a 2.8-µm-sized bead (large spherical signal) at 70s. **(b)** Space-time intensity plot (kymograph) of the QDs and the bead along the path of the motile microtubule in (a). **(c)** Intensity (red) and velocity (blue) traces vs. traveled distance for the QD marked with the arrow head in (a). The singular, broadened peak observed here (and in a few other examples) after initial cargo-pick-up was presumably caused by a slight sideways slippage of the cargo-attachment to the microtubule during the pick-up phase or the build-up of internal strain in the microtubule. **(d-f)** Images corresponding to (a-c) from another time series for the drop-off of a bead at 98s. The smaller satellite peaks (which occur in between the larger, 8-µm-spaced peaks) were most likely caused by a nearby second QD that gave rise to additional fluorescence signals. Such occasional high QD densities could be explained by the fact that microtubules in the cargo transport experiments were prepared with high biotinylation ratios in order to increase the number of events, where QD labeling coincided with cargo-loading on the same microtubule. Scale bars in (a) and (d) are 5 µm.

The missing impact of large cargo on the velocity of microtubules was surprising for a processive motor like kinesin-1 given that there was an indication of considerable axial load acting on the microtubule-bead composites. Thereby generated forces seem to be sufficient to break loose

cargo, which is less strongly bound than the 2.8 µm streptavidin-coated beads used here. When attempting to perform the same cargo pick-up experiments as described above with smaller beads of 1 µm in diameter only short periods of cargo transport could be observed, since the beads were released from the microtubules soon after loading. A possible explanation is that larger beads have a higher capacity to form multiple biotin-streptavidin links than smaller beads, which leads to a stronger binding of the large beads in total. Moreover, the conservation of the traveling speed of the microtubules concurs with previous observations that were made with a non-processive motor. In an earlier study [21] using monomeric, non-processive kinesin-1, it was shown that a long kinked structure at the microtubule end could block the rotary motion without effect on the forward speed. However, this behavior could be well explained by the possibility that a non-processive motor can always freely choose the nearest protofilament for the next step. In contrast, the data presented here are the first evidence of such behavior for dimeric, processive kinesin-1, which is assumed to follow the axis of an individual protofilament during its whole run. Therefore, this study might indicate that - when forced to do so - kinesin-1 might be able to switch protofilaments. Such switching might involve a short period of motor release from the microtubules, as the action of a sideways force on the motor-microtubule interaction is known to reduce kinesin's run length [120].

The fact that the velocity of microtubule gliding was almost not impacted shows that kinesin-driven microtubules make flexible, responsive and effective molecular shuttles for nanotransport applications. In addition, the results might indicate that *in vivo* kinesin-1 molecules, which transport cargo along microtubules, can likewise flexibly respond to an axial force by deviating from their path parallel to the protofilament axes.

3.6 22S Dynein-Induced Microtubule Rotation

The first microtubule motor protein, which has been demonstrated to be capable of exerting torque on a gliding microtubule is 14S dynein from

Tetrahymena cilia [18]. This was seen when the trailing ends of microtubules consisted of curved outer doublets or axonemes, thereby providing an asymmetric marker. In the same study, 22S dynein, also from *Tetrahymena* cilia, was characterized in terms of *in vitro* motility as well. While both motors induced translocation of microtubules with their plus-ends leading, interestingly 22S dynein could not be shown to cause rotation of microtubules. However, there is a more recent report where *Tetrahymena* 22S dynein is attributed the capability of generating torque similar to 14S dynein [19]. This observation was based upon supercoiling of microtubules in a gliding assay where the leading end of microtubules was stuck to the surface. The orientation of rotation of gliding microtubules was clockwise when looking in the direction of motion – the same as previously reported for 14S dynein [18].

Since *in vitro* axonemal dynein speeds [18, 19, 51-53] can be one order of magnitude faster than what has been described for kinesin-1 [37, 39] and cytoplasmic dynein [54, 55], they are promising candidates for fast transport tasks in nanotechnology applications. Therefore, it was of interest to resolve the controversial positions about torque generation of 22S dynein.

The interference-based 3-D tracking method was applied to investigate whether microtubules do rotate when gliding on an 22S dynein-coated silicon surface.

As seen in the case of kinesin-1, the maximum projection of the QD intensity over time directly reveals a periodic intensity signal (Figure 17a). The interpretation of the periodic intensity changes is a regular rotation of the QD carrying microtubule as well. In order to quantify the rotational pitches, QD positions were tracked for every frame, and the FLIC signal was plotted vs. traveled distance (Figure 17b). As Figure 17c shows, an average rotational pitch of 1.76 ± 0.4 µm (mean ± standard deviation) was obtained for 21 rotating microtubules.

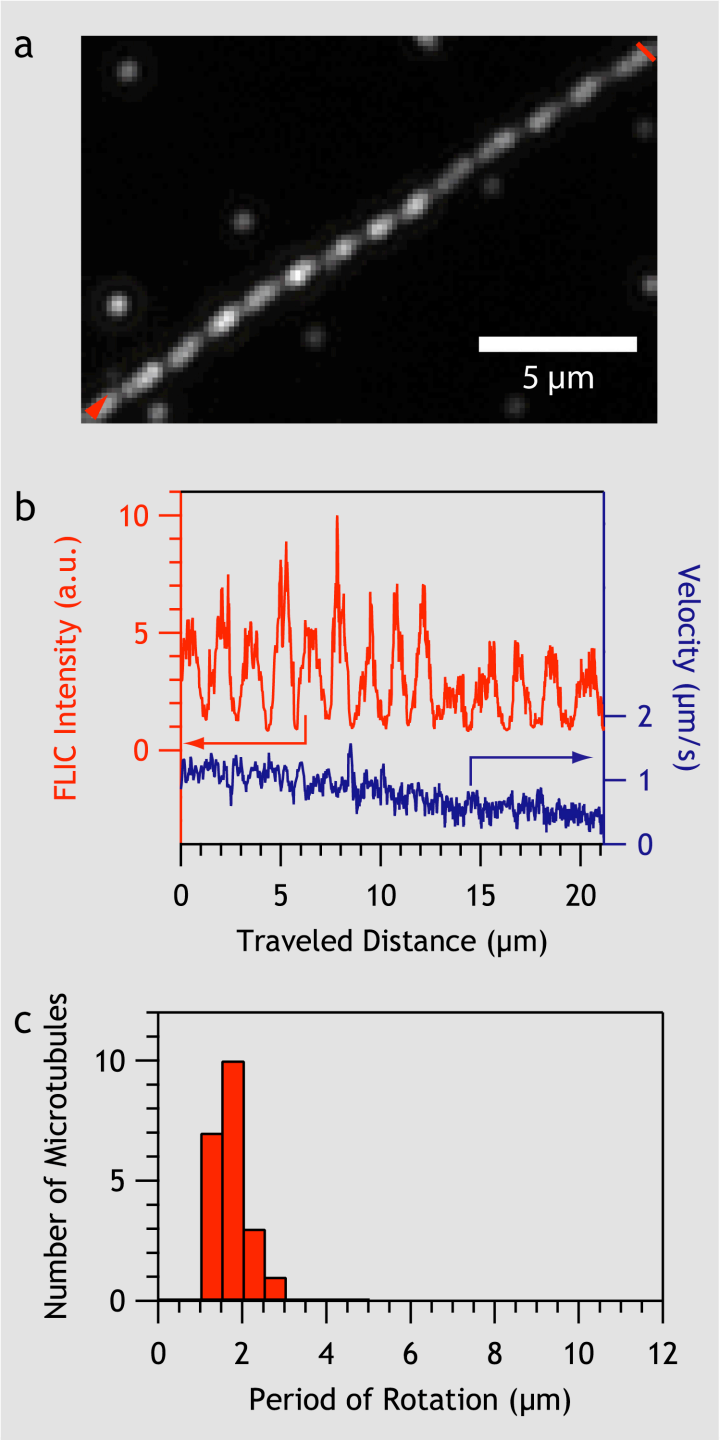

Figure 17: Microtubule rotation in 22S dynein gliding assay. FLIC microscopy of QDs attached to gliding microtubules driven by *Tetrahymena* 22S dynein. Imaging was performed at a rate of 20 fps using laser excitation. **(a)** Characteristic maximum projection of recorded QD signals over time. **(b)** Typical intensity (red) and velocity (blue) traces vs. traveled distance for a microtubule-attached QD. Data correspond to the marked maximum projection in (a). **(c)** Histogram of measured rotational periodicities on 22S dynein-coated surfaces (periodicity = 1.76 ± 0.4 µm, mean ± standard deviation, n = 21).

The fact, that 22S dynein induced microtubule rotations were observed in these experiments, is in contrast to the report of Vale and Toyoshima [18] and rather agrees with Mimori and Miki-Noumura [19]. The latter had concluded the presence of torque generation from supercoiling of tip-immobilized microtubules in a gliding geometry. This investigation of the rotational period of gliding microtubules here, however, is the first quantitative report about this issue.

The data suggest that unlike kinesin-1 the 22S dynein motors do not follow the protofilament axis of microtubules. If that was the case, the measured rotational pitch would only be consistent with microtubules comprising 11 protofilaments, which are predicted to feature a right-handed supertwist with a pitch of 1.7 µm [114]. However, this possibility can be ruled out, because so far neither the used nor any other *in vitro* preparation method of microtubules has been reported to predominantly cause the assembly of 11 protofilament microtubules.

When comparing the measured rotational pitch to the finding of about 0.5 µm per full rotation for 14S dynein [18], there is a factor of approximately three. So far, it is not clear whether this results from differences in motor properties or experimental conditions. A more detailed investigation of this issue was beyond the scope of this work, but would in principle be desirable. Interestingly, in another study off-axis movement of cytoplasmic dynein was observed in stepping assays [8]. Therefore, the absence of torque generation during ATP-induced interaction with microtubules has not been observed for any form of dynein so far.

It is certainly worthwhile to characterize 22S dynein in more detail from a biophysical point of view, in order to better understand how it contributes to the oscillating motions of flagella and cilia. However, the *in vitro* gliding assays with 22S dynein have turned out to be far less robust than for instance kinesin-1 gliding assays. In particular, gliding velocities were observed to vary between different experiments, ranging from below 0.5 µm/s up to ~5 µm/s. In addition, stop-and-go-like movement was often seen, where slow or stalled motion alternated. This observation is in agreement with previous reports from literature [51, 121, 122] and gives

reason to assume that controlled transport based on dynein is rather difficult to establish.

3.7 Ncd-Induced Microtubule Rotation

Since ncd is a microtubule minus-end-directed motor, it may be considered an alternative to the likewise minus-end-directed dynein within the scope of nanotransport systems. It is known that ncd can generate torque and cause the rotation of microtubules in gliding motility assays [20]. However, more detailed studies in this respect are missing. Therefore, it was of interest to apply 3-D nanometer tracking to further characterize microtubule rotation and implications for the potential of ncd in nanotransport using the gliding geometry.

At first, the rotation of gliding GMP-CPP microtubules at high surface densities of ncd (that allowed movement of sub-micrometer long microtubules) and saturating ATP was investigated. Figure 18a shows the maximum projection of a typical FLIC intensity trace of a QD attached to a gliding microtubule. Quantitative analysis was performed on the tracked positions and corresponding FLIC intensities (Figure 18b, c), yielding an average periodicity of 1.53 ± 0.52 µm (mean ± standard deviation, n = 36). As in the case of dynein, this value cannot be directly related to the structure of the microtubule lattice.

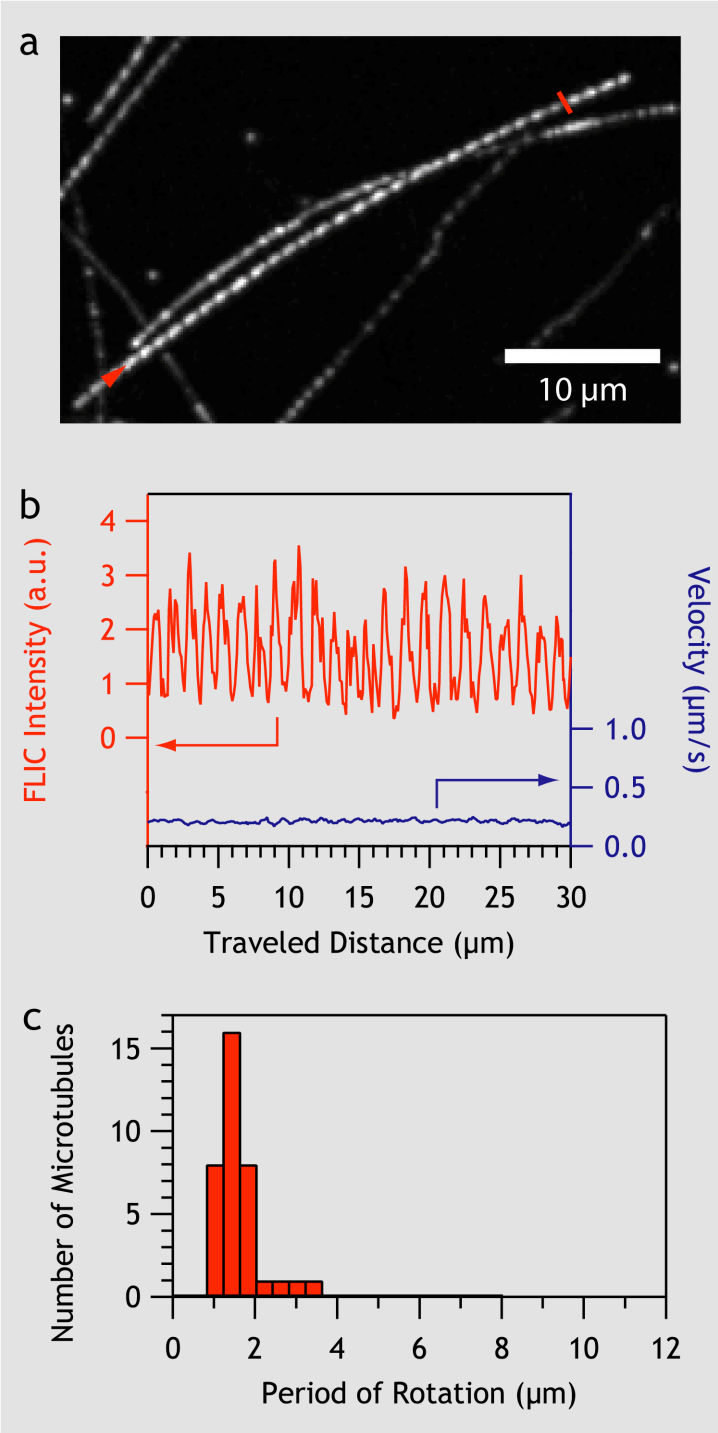

Figure 18: Microtubule rotation in ncd gliding assay. FLIC microscopy of QDs attached to gliding microtubules, which were driven by ncd. Imaging was performed at a rate of 1 fps (100 ms exposure) using laser excitation. **(a)** Characteristic maximum projection of recorded QD signals over time. **(b)** Typical intensity (red) and velocity (blue) traces vs. traveled distance for a microtubule-attached QD. Data correspond to the marked maximum projection in (a). **(c)** Histogram of measured rotational periodicities on ncd-coated surfaces (periodicity = 1.53 ± 0.52 µm, mean ± standard deviation, n = 36).

The experimental data confirm the presence of off-axis components in the power strokes of ncd motors consistent with previous work [20]. However, the rotational pitch does not agree with the previously reported value of ~0.3 µm [20]. So far, the reason is not clear. It could firstly be related to the experimental method. In the earlier report, microtubules were grown from axoneme fragments, which were introducing kinks at the microtubule ends that were trailing in gliding assays. Detection of microtubule rotation therefore relied on the observation of sideways flipping of the micrometer-sized axoneme tail, whose impact on microtubule rotation is not known. Another possibility could be that microtubule-attached QDs were causing an elongated period of rotation due to sticking on or friction with the surface. However, the width of the FLIC intensity peaks indicates that the distance of forward movement during the time when the QD is pointing away from the surface (and cannot disturb rotation) is already longer than the previously reported period of 0.3 µm for a full rotation. Furthermore, it would be expected that multiple QDs attached to gliding microtubules would affect rotation stronger than only one QD. There is no indication that this is the case. This still holds true when considering that non-emissive QDs may also bind to microtubules. The dark fraction of the QDs can be estimated based on their ensemble quantum yield [123]. In the case of the experiments here, the ensemble quantum yields of the QDs were between 50 and 60 % indicating that the fraction of non-radiant QDs was below 50 %. In addition, labeling of microtubules with QDs was sparse. Most of the microtubules had no or only one visible QD attached. Therefore, a substantial number of QDs should still have only one bright QD bound and no non-emissive one. Hence, it is unlikely that QDs have a detrimental effect on microtubule rotation in an ncd gliding assay. However, there is another important circumstance that has to be noted. While Walker et al. were performing their gliding assays in bacterial lysate with supplementation of ATP, the results in Figure 18 are based on experiments with purified ncd motor proteins in a reconstituted buffer. Maybe, the path, which the ncd motors choose on the microtubule lattice in the gliding situation, is generally not very stable and hence susceptible to

experimental conditions. This could provide an alternative explanation for the differences in the observed rotational periods. With regard to the application of ncd for nanotransport systems, it may thus be possible to influence or even control microtubule rotation in ncd gliding assays.

A well-adjustable parameter that is often used for speed control in gliding motility assays is the concentration of ATP that is powering the motor proteins. To test the effect of ATP concentration on the rotation of microtubules, the ATP concentration was gradually reduced from 700 µM to 210 µM to 70 µM, and finally adjusted back to 700 µM during gliding motility assays. The effect was surprisingly dramatic, as can be seen in the example of a typical FLIC intensity trace of a QD attached to a gliding microtubule (Figure 19a). When the ATP concentration was reduced (i) a corresponding velocity decrease and (ii) a corresponding decrease in length of the rotational pitches were observed. Moreover, the graphs show that the effect is reversible when switching back to high ATP concentrations. Figure 19b shows the rotational pitches of 7 microtubules over the time course of the experiment at the different ATP concentrations. Data were obtained from the same sample as the example trace (Figure 19a). It is important to note that the temporal frequency of microtubule rotation was affected as well. It was lowest for the lowest tested ATP concentration of 70 µM.

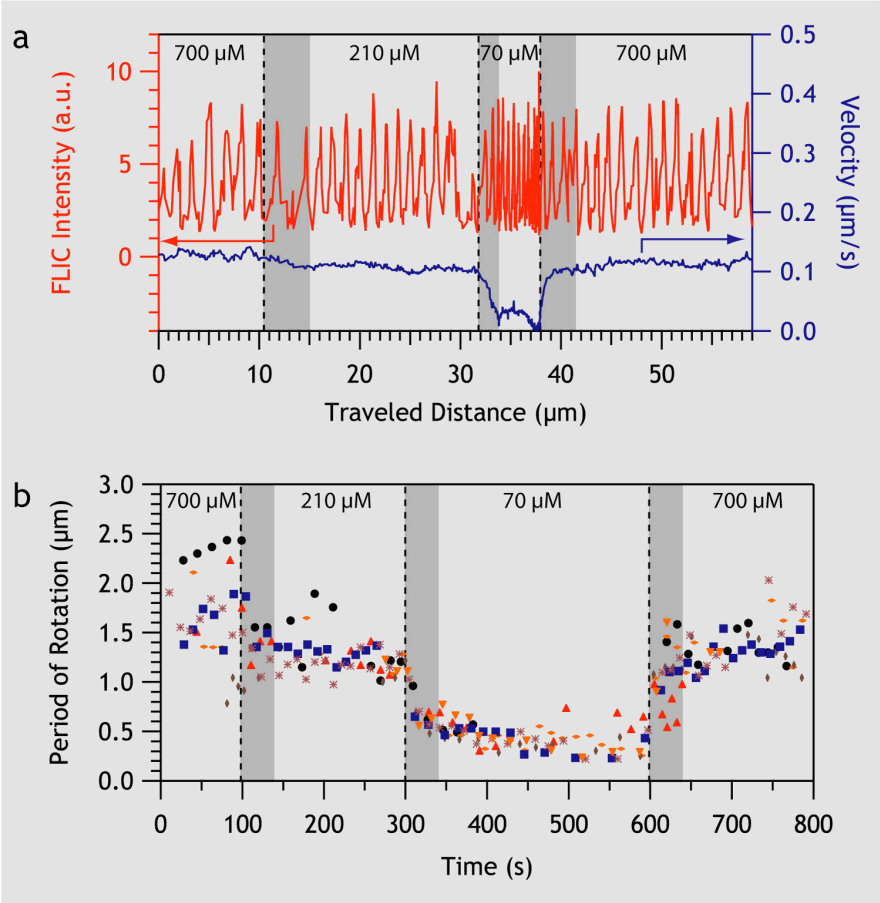

Figure 19: Influence of ATP concentration on rotation of microtubules gliding over an ncd-coated surface. ATP concentration was varied while FLIC microscopy was being performed on QDs 655 attached to gliding microtubules. The initial motility solution with 700 µM ATP was exchanged after 100 s, 300 s and 600 s for motility solutions with 210 µM, 70 µM and 700 µM ATP, respectively. The grey bars indicate the duration of the exchange process. Fluorescence excitation was performed by arc lamp illumination. Image acquisition rate was 1 fps with 100 ms exposure time. **(a)** Example of intensity (red) and velocity (blue) traces vs. traveled distance for a microtubule-attached QD. **(b)** Rotational periods of 7 microtubules over time from the same flow chamber as the example from (a). The average rotational pitches at the different ATP concentrations from left to right: 1.84 ± 0.9 µm (n=99); 1.26 ± 0.19 µm (n=43); 0.42 ± 0.12 µm (n=68); 1.33 ± 0.18 µm (n=39) (all mean ± standard deviation (n = number of periods)). Periods during exchange of solutions were not considered.

What is the reason for this spectacular behavior? So far ncd has been reported to be non-processive [65-67], except for one recent report [68].

For the latter, it is not clear to which extend the observation is caused by the involvement of the ATP-insensitive microtubule binding site of ncd or the particular experimental conditions (such as low salt concentration) used. Possibly, the processively moving ncd motors were clusters of motors as a study from our laboratory suggests [G. Fink, personal communication]. Consequently, it is assumed that ncd detaches after each powerstroke from the microtubule and eventually rebinds to the microtubule. When ncd is waiting to bind to the microtubule, it is supposed to be in an ADP-bound state. Subsequently, it weakly binds in the ADP state and switches to a nucleotide-free state upon ADP release [124]. Therefore, the time until binding to microtubules should be independent of ATP concentration. This is different for the microtubule-bound state. Here, it is more likely at high ATP concentrations that ATP binds to an ncd molecule in the microtubule-bound rigor state and a subsequent powerstroke occurs. This has been confirmed experimentally by trapping experiments where the ncd detachment lifetimes were observed to decrease with increasing ATP concentration [65]. Taken together, this means that the duty ratio [23] of ncd is changing with ATP concentration, because at low ATP concentration the motor spends an increasing amount of time bound to microtubules in the nucleotide-free pre-powerstroke state. How does this translate to a gliding motility assay with variable ATP concentration? With decreasing ATP concentration, the number of motors that on average are bound to a gliding microtubule in the nucleotide–free pre-powerstroke state is increasing. This is true for total numbers, as well as in proportion to the number of motors in any microtubule-bound states other than the nucleotide-free pre-powerstroke. The observation of shorter rotational pitches is compatible with the notion that the pre-powerstroke state impedes forward motion of the microtubule more strongly than its rotation. While so far, it is unclear what the implication for the *in vivo* function of ncd might be, the effect is interesting for nanotransport. The tuning of rotations of microtubule shuttles might offer a means for enhanced cargo pick-up. In particular, higher and more homogeneous cargo densities on the surface of the filaments might be achievable because the effective surface area of the

filaments exposed to loading stations that are passed by gliding microtubules can be increased.

In conclusion, ncd has been confirmed to generate torque. Moreover, this effect has been found to depend on ATP concentration, something, which might possibly be exploited when designing nanotransport systems.

4 Summary and Outlook

The aim of this work was to develop a method to characterize the behavior of filamentous nanoshuttles – specifically of motor protein-driven microtubules – in 3-D. The main requirements to meet were low impact on the nanotransport system, high spatial and temporal resolution, and versatility. Furthermore, this method was intended to be used to address open questions in the field of nanotransport. In particular, it was firstly attempted to characterize cargo transport in a system currently favored by most studies in the field, where nanoshuttles are powered by the microtubule motor best understood so far – the plus-end-directed kinesin-1. Secondly, the goal was to further the understanding of potential counter-players of kinesin-1 in nanotransport applications - the much less well understood microtubule minus-end-directed motor proteins 22S dynein and ncd.

A novel method to study the linear forward motion as well as the axial motion of filamentous nanoshuttles, which are driven by motors of the cell cytoskeleton, has been introduced. The method uses fluorescence interference-based 3-D nanometer tracking of QDs as optical probes that are attached to the nanoshuttles. While other recently reported 3-D tracking techniques based on dual-focus imaging offer similar sensitivity, the method here can be easily performed on any standard epi-fluorescence microscope, even with arc lamp illumination, and additionally holds the potential to retrieve absolute height values. It is strongly suggested that the ease of use might help to spread this valuable and versatile tool for a variety of applications, including studies of interactions between single molecules or even intramolecular changes.

Specifically, 3-D tracking has been used to visualize and analyze the rotation of microtubules around their longitudinal axis when they are propelled on a motor protein-coated surface. This geometry called gliding assay is currently favored for most proof-of-principle studies that investigate the use of biomolecular motors for transport of nanoscale cargo

with the goal to assemble and manipulate nanostructures. The suitability of the method has been proven for kinesin-1 gliding assays, where knowledge of properties of both, microtubules and kinesin-1, allowed a very precise prediction of microtubule rotation, which was matching the actual measured values very well.

The microtubule rotation in kinesin-1 gliding assays has turned out to be robust against the attachment of small cargo in the shape of QDs, but also against the reduction of electrostatic interactions between microtubules and kinesin-1 by cleavage of the tubulin E-hook. The situation was dramatically different when large cargo was attached to microtubules. In this case, filament rotation was stopped, but otherwise the impact on motility was surprisingly low. In particular, the velocity of the gliding microtubules only decreased to a negligible degree. This shows that in principle microtubules driven by processive motors like kinesin-1 can make flexible, responsive and effective molecular shuttles for nanotransport applications. In addition, the results might indicate that *in vivo* kinesin-1 molecules, which transport cargo along microtubules, can likewise flexibly respond to an axial force by deviating from their path parallel to the protofilament axes.

Two microtubule minus-end-directed motors that might be employed to counteract kinesin-1 in engineered nanotransport systems are dynein and ncd. Both motors have been found to be capable of generating torque causing short-pitched microtubule rotation in gliding motility assays. The results for 22S dynein helped to resolve controversial findings of earlier reports about the ability of 22S dynein to generate torque. However, it turned out difficult to establish conditions where the movement of the dynein-driven nanoshuttles was homogeneous and reproducible. In contrast, motility in ncd gliding assays looks much more promising. The obtained results supported previous reports of torque generation by ncd. Moreover, a strong dependence of rotational pitches of gliding microtubules on ATP concentration was found. The reason could be that ncd motors in the nucleotide-free microtubule-bound state impede the forward movement of gliding microtubules stronger than the axial motion. To fully understand the

nature of this effect, further research is required. Most likely, this will substantially contribute to the understanding of ncd function *in vivo*. Furthermore, the possibility of tuning the rotation of microtubules acting as nanoshuttles might provide a means to increase control of processes like cargo-loading and unloading.

5 Materials and Methods

5.1 Microtubules

Bovine and porcine tubulin were used for microtubule self-assembly. All bovine tubulin was purchased from Cytoskeleton. Porcine tubulin was purified from pig brain and partly labeled with Alexa 488 (Invitrogen) as described previously [125].

GMP-CPP microtubules were grown for 2 hours at 37˚C from a 100 µl BRB80 (80 mM Pipes [Sigma], pH 6.9 adjusted with KOH [VWR], 1 mM ethylene glycol-bis (2-aminoethylether)-N,N,N',N'-tetra acetic acid [EGTA; Sigma], 1 mM $MgCl_2$ [VWR]) solution supplemented with 2 µM tubulin (53 % unlabeled porcine, 45 % Alexa 488 labeled porcine, 2 % biotinylated bovine tubulin for Chapters 3.2 and 3.3; 94 % unlabeled, 3 % rhodamine labeled, 3 % biotinylated bovine tubulin for Chapter 3.4; 45 % unlabeled, 10 % rhodamine labeled, 45 % biotinylated bovine tubulin for Chapter 3.5; 94.5 % unlabeled, 5 % rhodamine labeled and 0.5 % biotinylated bovine tubulin for Chapter 3.6; 78 % unlabeled, 20 % rhodamine labeled and 2 % biotinylated bovine tubulin for Chapter 3.7), 1 mM GMP-CPP (Jena Bioscience), 4 mM $MgCl_2$.

BRB80 + Taxol microtubules were grown for 3 hours at 37˚C from a 100 µl BRB80 solution supplemented with 2 µM tubulin (53 % unlabeled porcine, 45 % Alexa 488 labeled porcine, 2 % biotinylated bovine tubulin), 0.5 mM Mg-GTP (Roche), 4 mM $MgCl_2$, and 10 µM Taxol (Sigma).

BRB80 + DMSO microtubules were grown for 30 minutes at 37˚C from a 6.25 µl BRB80 solution supplemented with 32 µM tubulin (94.5 % unlabeled, 5 % rhodamine labeled and 0.5 % biotinylated bovine tubulin), 1 mM Mg-GTP, 4 mM $MgCl_2$, and 5 % DMSO (Sigma). Microtubules were then diluted and stabilized in 500 µl BRB80 buffer supplemented with 10 µM taxol.

Assembled GMP-CPP, BRB80 + Taxol, and BRB80 + DMSO microtubules were separated from free tubulin by centrifugation in a Beckman Airfuge at 100,000 g for 5 min. The pellet was resuspended in a volume of 50 - 500 µl

BRB80 supplemented with 10 µM taxol. The final tubulin concentrations were 0.4 – 4 µM.

BRB80 microtubules were grown for 45 minutes at 37˚C from a 6.7 µl BRB80 solution supplemented with 50 µM tubulin (74 % unlabeled, 22 % rhodamine labeled and 4 % biotinylated bovine tubulin) and 1 mM Mg-GTP. Microtubules were then diluted and stabilized in 500 µl BRB80 buffer supplemented with 10 µM docetaxel (Sigma).

MES + DMSO microtubules were grown for 30 minutes at 37˚C from a 10 µl MES (100 mM MES potassium salt, pH 6.5 adjusted with HCl, 1 mM $MgCl_2$, 1 mM EGTA) solution supplemented with 50 µM tubulin (88 % unlabeled, 10 % rhodamine labeled and 2 % biotinylated bovine tubulin, 1 mM Mg-GTP, 4 mM $MgCl_2$, and 5 % DMSO. Microtubules were then diluted and stabilized in 500 µl MES buffer supplemented with 10 µM docetaxel.

Biotinylation of microtubules: Assembled microtubules were biotinylated by adding 5 µl of 180 µM EZ-Link NHS-LC-LC-Biotin (Pierce) in DMSO to 400 µl resuspended microtubule solution and incubated at 37˚C for 30 min followed by incubation with 25 mM Potassium glutamate (Sigma) for 10 min. The whole volume was centrifuged for 5 min at 100,000 g in a Beckman Airfuge and resuspended in 400 µl of BRB80. Both steps (centrifugation and subsequent resuspension) were repeated twice.

Subtilisin digestion of microtubules: GMP-CPP microtubules (95 % unlabeled, 2 % rhodamine labeled and 3 % biotinylated bovine tubulin) were incubated with 10 µg/ml subtilisin (Sigma) for 20 min at 37˚C. Subsequently, 5 mM phenylmethanesulphonylfluoride (PMSF; Sigma; from 0.5 M stock solution in ethanol [VWR]) was added to stop the reaction. The digested microtubules were then centrifuged for 5 min at 100,000 g in a Beckman Airfuge over a 40 % glycerol-BRB80 cushion (containing 6 µM Taxol; glycerol from VWR) and redissolved in BRB80 with 10 µM Taxol to a final concentration of 400 nM assembled tubulin.

5.2 Motor Proteins

The following motor proteins were used: full length *Drosophila melanogaster* kinesin-1 that was expressed in *Escherichia coli* and purified applying published protocols [126], *Tetrahymena* 22S dynein (a kind gift of Yuuko Wada and Peter Satir, Albert Einstein College of Medicine of Yeshiva University, New York, USA), and full length *Drosophila melanogaster* kinesin-14 (ncd, nonclaret-disjunctional, which was a kind gift of Lukasz Hajdo and Andrzej A. Kasprzak, Nencki Institute Warsaw, Poland).

5.3 In Vitro Motility Assays

5.3.1 Flow Cells

All gliding motility assays were performed in microfluidic flow cells, which consisted of glass coverslips and silicon wafers separated by a thin spacer. Generally, 22 x 22 mm glass coverslips (Corning, No 1.5), 10 x 10 mm silicon wafers with a thermal oxide layer of 30 - 35 nm (GESIM; 90 nm oxide layer for the dynein experiments), and parafilm (Pechiney) or double sided tape (3M Scotch) as spacer were used for construction of the flow cells (10 mm x 1.5 mm x 0.05 – 0.15 mm). For the cargo pick-up and drop-off experiments, flow cells (18 mm x 1.5 mm x 0.1 mm) were made of 23 x 10 mm silicon wafers (30 nm thermal oxide layer) and 18 x 18 mm glass coverslips. Before use silicon wafers were washed in acetone (VWR), sonicated in mucasol (VWR; 1:20 dilution in water) for 15 min, sonicated in ethanol for 10 min, rinsed in double distilled water and blown dry with nitrogen. Coverslips were either pegylated (for the dynein, ncd, and cargo pick-up / drop-off experiments; see ref. [127] for pegylation procedure) or cleaned by the same procedure as the silicon wafers, but without acetone washing (in all other cases).

5.3.2 Kinesin-1 Gliding Motility Assay

Flowcell surfaces were blocked by perfusion of a 0.5 mg/ml casein (Sigma) solution in BRB80. After 5 min a kinesin-1 solution (100 µg/ml kinesin-1, 10 µM to 1 mM ATP [Roche], 0.2 mg/ml casein in BRB80) was perfused through the channel. Another 5 min later the microtubule solution containing 10 µM to 1mM ATP, 10 µM taxol and 0.2 mg/ml casein in BRB80 was perfused through and microtubules were allowed to bind to the motors for about 5 min. Subsequently, 10 µl of a QD 655 (Invitrogen) containing solution (BRB80, 10 µM to 1 mM ATP, 10 µM taxol, 0.2 mg/ml casein, 2 pM to 50 pM QD 655) was perfused through. After 5 to 10 min of incubation, excess QDs were washed out with 60 - 100 µl of a motility solution (BRB80, 10 µM to 1 mM ATP, 10 µM taxol, 0.2 mg/ml casein, and an oxygen scavenger mix of 20 mM D-glucose [Sigma], 0.02 mg/ml glucose oxidase, 0.008 mg/ml catalase, and 10 mM DTT or 0.5 % BME [all from Sigma]). For the cargo pick-up and drop-off experiments, Dynabeads M-270 streptavidin (0.03 to 0.1 pM, Dynal, Invitrogen) in motility solution with 1 mM ATP were additionally perfused into the flow chamber.

In the cases where gliding assays were performed using BRB80 microtubules and MES + DMSO microtubules, microtubule-containing solutions were supplemented with 10 µM docetaxel instead of 10 µM taxol to preserve the stability of the microtubules.

5.3.3 22S Dynein Gliding Motility Assay

The flow chamber was first rinsed with a 22S dynein specific motility buffer (10 mM TRIS acetate, 3 mM $MgSO_4$, 2 mM EGTA (pH 7.5) supplemented with 2 mM DTT and 50 mM potassium acetate (pH 6.3)). Subsequently, dynein (100 µg/ml) was perfused into the flowcell and allowed to bind to the surface for 5 minutes. The flow cell content was then exchanged for a mixture of 50 µg/ml dynein along with 1 mg/ml casein in motility buffer. After an incubation period of 5 minutes, excess protein was washed out with 60 µl motility buffer. Then, a microtubule-containing motility solution (tubulin content ~80 nM; GMP-CPP microtubules or BRB80 + DMSO

microtubules) consisting of motility buffer supplemented with 10 µM Taxol, 0.7 mM ATP, and 10 µM ADP were allowed to flow into the channel. After 5 minutes a solution with ~40 pM QD 655 particles consisting of motility buffer supplemented with 10 µM Taxol, 0.7 mM ATP, and 10 µM ADP was replacing the flow cell content. QDs were allowed to bind to microtubules for 5 minutes before they were washed out with a motility solution (without microtubules) consisting of motility buffer supplemented with 10 µM Taxol, 0.7 mM ATP, 10 µM ADP, and an oxygen scavenger mix (20 mM D-glucose, 0.02 mg/ml glucose oxidase, 0.008 mg/ml catalase, and 10 mM DTT). Subsequently, imaging was performed.

5.3.4 Ncd Gliding Motility Assay

Flowcells were incubated with 1 mg/ml Protein A (Sigma) in BRB20 (20 mM Pipes, pH 6.9 adjusted with KOH, 1 mM EGTA, 1 mM $MgCl_2$) for 20 minutes. The channels were then washed with 60 µl of a washing buffer (BRB20 pH 6.9, 75 mM KCl, 0.7 mM ATP, 0.5 mg/ml casein). Then ncd motors (20 µg/ml except 200 µg/ml for Figure 18c) in washing buffer were perfused into the flow chamber and washed out with 100 µl washing buffer after 5 minutes. Next, microtubules diluted in washing buffer with 10 µM taxol were flown into the chamber. After 5 minutes 5 pM to 20 pM QDs 655 in washing buffer with 10 µM taxol (and only 0.1 mg/ml casein) were perfused into the flow channel and allowed to bind for 10 minutes. QDs were finally washed out by a motility solution containing an oxygen scavenger system (BRB20, 75 mM KCl [Sigma], 10 µM Taxol, 0.7 mM ATP, 0.2 mg/ml casein, and an oxygen scavenger mix of 20 mM D-glucose, 0.02 mg/ml glucose oxidase, 0.008 mg/ml catalase, and 0.5 % BME). The same motility solution, but with varying ATP concentrations of 0.21 mM and 0.07 mM, was used in the case of Figure 19 when motility solution was exchanged during imaging.

5.4 Data Acquisition and Analysis

5.4.1 Optical Imaging

Image acquisition was performed using an inverted fluorescence microscope (Zeiss Axiovert 200M) with 63x water immersion 1.2 NA or Fluar 100x 1.45 NA (only for dynein experiments) objectives (Zeiss) in combination with an Andor Ixon DV 897 (Andor) EMCCD camera (unless stated otherwise). Filters and dichromatic mirrors used were from Chroma Technology unless stated otherwise.

Fixed Objects: Imaging in FLIC-mode was performed using a 63x water immersion objective (optovar 1.6; i.e. camera pixel size 160 nm). Fluorescent excitation was achieved by arc lamp (Lumen 200 metal arc lamp, Prior Scientific Instruments Ltd.) or laser (488 nm line of an argon/krypton ion laser, 50 mW optical power, Coherent Innova 70C Spectra) illumination. The filter sets for arc lamp illumination were identical with the ones described below for the imaging of gliding assays with single color detection. The following filters were used during laser excitation: exc 488/10, dc 505 LP, em 660/40 and em 531/40 (Semrock) for QDs and yellow-green fluorescent beads, respectively.

Imaging of gliding assays: For excitation either a Lumen 200 metal arc lamp (Prior Scientific Instruments Ltd.) or the 488 nm line of an argon ion laser (Coherent Innova 70C Spectra) was used. Cargo pick-up and drop-off experiments were performed on an upright fluorescence microscope (Zeiss Axioplan 2) using a Plan-Neofluar 40x oil immersion 1.3 NA objective (Zeiss). Images were recorded in continuous acquisition mode at rates of up to 20 fps or in case of the ncd experiments as time series with 1 fps and 100 ms exposure. For experiments that involved dual-color imaging, i.e. when the fluorescence signals of QDs and microtubules were to be captured simultaneously, the red and the green channels were separated employing a spectral beam splitter (W-view A8509, Hamamatsu). The signals of the two color channels were then recorded on two different halves of the same CCD camera chip (Figure 20). To align the dual-color images with respect to each

other, multifluorescent tetraspeck beads (0.2 µm diameter, Mo Bi Tec) were diluted 200-fold in BRB80 and additionally perfused into the flow chambers prior to the flow sequence of the motility assays. The following filters were used for imaging when arc lamp illumination was used: exc 475/42 (Semrock), dc 488LP (Semrock), and em dual-band 527-645 (Semrock) for dual-color detection. In addition, the W-view beamsplitter was equipped with: em 531/40 (Semrock), em 660/40, dc 590dcxr, and dc Q590dcspxr. For single-color detection either the green or the red detection path of the W-view beamsplitter were used while the dichromatic mirrors were replaced by a silver mirror. For cargo pick-up and drop-off experiments no W-view beamsplitter was installed and a single band emission filter em 660/40 was used instead of the em dual-band 527-645 (Semrock). When 488 nm laser excitation was applied the following filters were used for single color detection: exc 488/10, dc 505 LP, em 660/50.

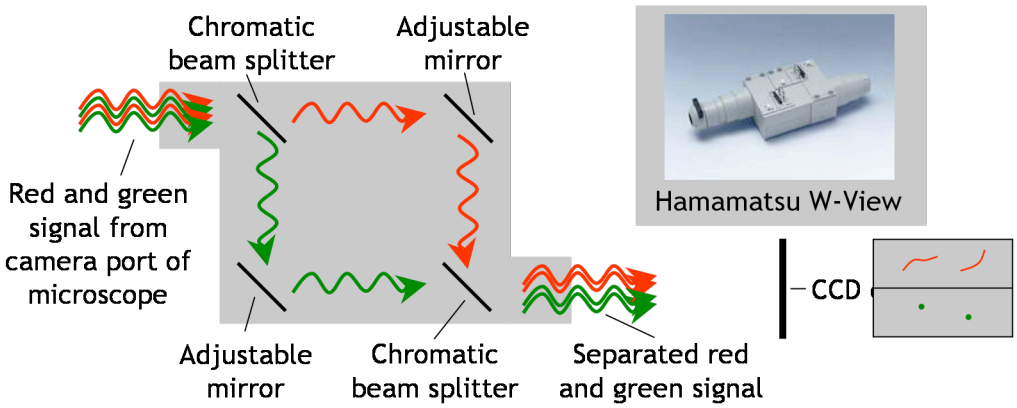

Figure 20: Instrumentation for color separation of dual-color imaging. The dual-color signal from the camera port of the microscope is split by a dichromatic mirror into its components and guided via adjustable mirrors to another dichromatic mirror. At this point the two colors of the signal are spatially separated but aligned thereby being detectable on two different halves of the CCD camera chip.

Image Processing: Single particle tracking was performed using an in-house software based on MatLab (Mathworks, Natick, MA). The applied algorithm used 2-D Gaussian fitting (least squares method; variable width of Gaussian) of the pixilated intensity profiles arising from single particles.

Plotted FLIC intensity values were derived by integration over the fitted Gaussians. Microtubule tracking was performed by segmentation of the filament images and consequent fitting by various Gaussian-based model functions. Rotational periodicities for the histograms were derived from manual, computer-aided measurements applied to the traces of FLIC intensity vs. traveled distance. The sideways deviation was calculated as the orthogonal distance between the QD positions and the centerline of the tracked microtubules.

Bibliography

[1] Drexler, K. E. 1992. Nanosystems: molecular machinery, manufacturing, and computation. Wiley, New York.

[2] Drexler, K. E., J. Randall, S. Corchnoy, A. Kawczak, and M. L. Steve. 2007. Productive Nanosystems A Technology Roadmap. http://www.foresight.org/roadmaps/Nanotech_Roadmap_2007_main.pdf.

[3] Shirai, Y., A. J. Osgood, Y. M. Zhao, K. F. Kelly, and J. M. Tour. 2005. Directional control in thermally driven single-molecule nanocars. Nano Lett. 5:2330-2334.

[4] Badjic, J. D., V. Balzani, A. Credi, S. Silvi, and J. F. Stoddart. 2004. A molecular elevator. Science 303:1845-1849.

[5] Gelles, J., B. J. Schnapp, and M. P. Sheetz. 1988. Tracking kinesin-driven movements with nanometre-scale precision. Nature 331:450-453.

[6] Svoboda, K., C. F. Schmidt, B. J. Schnapp, and S. M. Block. 1993. Direct observation of kinesin stepping by optical trapping interferometry. Nature 365:721-727.

[7] Seitz, A., and T. Surrey. 2006. Processive movement of single kinesins on crowded microtubules visualized using quantum dots. EMBO J. 25:267-277.

[8] Reck-Peterson, S. L., A. Yildiz, A. P. Carter, A. Gennerich, N. Zhang, and R. D. Vale. 2006. Single-molecule analysis of dynein processivity and stepping behavior. Cell 126:335-348.

[9] Vale, R. D., T. Funatsu, D. W. Pierce, L. Romberg, Y. Harada, and T. Yanagida. 1996. Direct observation of single kinesin molecules moving along microtubules. Nature 380:451-453.

[10] Yildiz, A., J. N. Forkey, S. A. McKinney, T. Ha, Y. E. Goldman, and P. R. Selvin. 2003. Myosin V walks hand-over-hand: single fluorophore imaging with 1.5-nm localization. Science 300:2061-2065.

[11] Yildiz, A., M. Tomishige, R. D. Vale, and P. R. Selvin. 2004. Kinesin walks hand-over-hand. Science 303:676-678.

[12] Hess, H., G. D. Bachand, and V. Vogel. 2004. Powering nanodevices with biomolecular motors. Chemistry 10:2110-2116.

[13] van den Heuvel, M. G., and C. Dekker. 2007. Motor proteins at work for nanotechnology. Science 317:333-336.

[14] Brunner, C., C. Wahnes, and V. Vogel. 2007. Cargo pick-up from engineered loading stations by kinesin driven molecular shuttles. Lab Chip 7:1263-1271.

[15] Ramachandran, S., K. H. Ernst, G. D. Bachand, V. Vogel, and H. Hess. 2006. Selective loading of kinesin-powered molecular shuttles with protein cargo and its application to biosensing. Small 2:330-334.

[16] Nishizaka, T., T. Yagi, Y. Tanaka, and S. Ishiwata. 1993. Right-Handed Rotation of an Actin Filament in an Invitro Motile System. Nature 361:269-271.

[17] Ray, S., E. Meyhofer, R. A. Milligan, and J. Howard. 1993. Kinesin follows the microtubule's protofilament axis. J. Cell Biol. 121:1083-1093.

[18] Vale, R. D., and Y. Y. Toyoshima. 1988. Rotation and translocation of microtubules in vitro induced by dyneins from Tetrahymena cilia. Cell 52:459-469.

[19] Mimori, Y., and T. Miki-Noumura. 1995. Extrusion of rotating microtubules on the dynein-track from a microtubule-dynein gamma-complex. Cell Motil. Cytoskeleton 30:17-25.

[20] Walker, R. A., E. D. Salmon, and S. A. Endow. 1990. The Drosophila claret segregation protein is a minus-end directed motor molecule. Nature 347:780-782.

[21] Yajima, J., and R. A. Cross. 2005. A torque component in the kinesin-1 power stroke. Nat. Chem. Biol. 1:338-341.

[22] Alberts, B., A. Johnson, J. Lewis, M. Raff, K. Roberts, and P. Walter. 2002. Molecular biology of the cell. Garland Science, New York.

[23] Howard, J. 2001. Mechanics of Motor Proteins and the Cytoskeleton. Sinauer Associates, Sunderland, MA.

[24] Schliwa, M., and G. Woehlke. 2003. Molecular motors. Nature 422:759-765.

[25] Wade, R. H., P. Meurer-Grob, F. Metoz, and I. Arnal. 1998. Organisation and structure of microtubules and microtubule-motor protein complexes. Eur. Biophys. J. 27:446-454.

[26] Meurer-Grob, P., J. Kasparian, and R. H. Wade. 2001. Microtubule structure at improved resolution. Biochemistry 40:8000-8008.

[27] Pierson, G. B., P. R. Burton, and R. H. Himes. 1978. Alterations in number of protofilaments in microtubules assembled in vitro. J. Cell Biol. 76:223-228.

[28] Amos, L. A., and D. Schlieper. 2005. Microtubules and maps. Adv. Protein Chem. 71:257-298.

[29] Howard, J., and A. A. Hyman. 2003. Dynamics and mechanics of the microtubule plus end. Nature 422:753-758.

[30] Morrison, E. E. 2007. Action and interactions at microtubule ends. Cell. Mol. Life Sci. 64:307-317.

[31] Goldstein, L. S., and Z. Yang. 2000. Microtubule-based transport systems in neurons: the roles of kinesins and dyneins. Annu. Rev. Neurosci. 23:39-71.

[32] Kozielski, F., S. Sack, A. Marx, M. Thormahlen, E. Schonbrunn, V. Biou, A. Thompson, E. M. Mandelkow, and E. Mandelkow. 1997. The crystal structure of dimeric kinesin and implications for microtubule-dependent motility. Cell 91:985-994.

[33] de Cuevas, M., T. Tao, and L. S. Goldstein. 1992. Evidence that the stalk of Drosophila kinesin heavy chain is an alpha-helical coiled coil. J. Cell Biol. 116:957-965.

[34] Amos, L. A. 1987. Kinesin from pig brain studied by electron microscopy. J. Cell Sci. 87 (Pt 1):105-111.

[35] Hirokawa, N., K. K. Pfister, H. Yorifuji, M. C. Wagner, S. T. Brady, and G. S. Bloom. 1989. Submolecular domains of bovine brain kinesin identified by electron microscopy and monoclonal antibody decoration. Cell 56:867-878.

[36] Schnitzer, M. J., and S. M. Block. 1997. Kinesin hydrolyses one ATP per 8-nm step. Nature 388:386-390.

[37] Coy, D. L., M. Wagenbach, and J. Howard. 1999. Kinesin takes one 8-nm step for each ATP that it hydrolyzes. J. Biol. Chem. 274:3667-3671.

[38] Block, S. M., L. S. Goldstein, and B. J. Schnapp. 1990. Bead movement by single kinesin molecules studied with optical tweezers. Nature 348:348-352.

[39] Howard, J., A. J. Hudspeth, and R. D. Vale. 1989. Movement of microtubules by single kinesin molecules. Nature 342:154-158.

[40] Asbury, C. L., A. N. Fehr, and S. M. Block. 2003. Kinesin moves by an asymmetric hand-over-hand mechanism. Science 302:2130-2134.

[41] Kaseda, K., H. Higuchi, and K. Hirose. 2003. Alternate fast and slow stepping of a heterodimeric kinesin molecule. Nat. Cell Biol. 5:1079-1082.

[42] Schief, W. R., R. H. Clark, A. H. Crevenna, and J. Howard. 2004. Inhibition of kinesin motility by ADP and phosphate supports a hand-over-hand mechanism. Proc. Natl. Acad. Sci. USA 101:1183-1188.

[43] Svoboda, K., and S. M. Block. 1994. Force and velocity measured for single kinesin molecules. Cell 77:773-784.

[44] Meyhofer, E., and J. Howard. 1995. The force generated by a single kinesin molecule against an elastic load. Proc. Natl. Acad. Sci. USA 92:574-578.

[45] Visscher, K., M. J. Schnitzer, and S. M. Block. 1999. Single kinesin molecules studied with a molecular force clamp. Nature 400:184-189.

[46] Gibbons, I. R., and A. J. Rowe. 1965. Dynein: A Protein with Adenosine Triphosphatase Activity from Cilia. Science 149:424-426.

[47] Brady, S. T. 1985. A novel brain ATPase with properties expected for the fast axonal transport motor. Nature 317:73-75.

[48] Vale, R. D., T. S. Reese, and M. P. Sheetz. 1985. Identification of a novel force-generating protein, kinesin, involved in microtubule-based motility. Cell 42:39-50.

[49] Vale, R. D., B. J. Schnapp, T. S. Reese, and M. P. Sheetz. 1985. Movement of organelles along filaments dissociated from the axoplasm of the squid giant axon. Cell 40:449-454.

[50] Oiwa, K., and H. Sakakibara. 2005. Recent progress in dynein structure and mechanism. Curr. Opin. Cell Biol. 17:98-103.

[51] Mimori, Y., and T. Miki-Noumura. 1994. ATP-induced sliding of microtubules on tracks of 22S dynein molecules aligned with the same polarity. Cell Motil. Cytoskeleton 27:180-191.

[52] Paschal, B. M., S. M. King, a. G. Moss, C. a. Collins, R. B. Vallee, and G. B. Witman. 1987. Isolated flagellar outer arm dynein translocates brain microtubules in vitro. Nature 330:672-674.

[53] Yokota, E., and I. Mabuchi. 1994. C/A dynein isolated from sea urchin sperm flagellar axonemes. Enzymatic properties and interaction with microtubules. J. Cell Sci. 107 (Pt 2):353-361.

[54] Paschal, B. M., H. S. Shpetner, and R. B. Vallee. 1987. MAP 1C is a microtubule-activated ATPase which translocates microtubules in vitro and has dynein-like properties. J. Cell Biol. 105:1273-1282.

[55] Toba, S., T. M. Watanabe, L. Yamaguchi-Okimoto, Y. Y. Toyoshima, and H. Higuchi. 2006. Overlapping hand-over-hand mechanism of single molecular motility of cytoplasmic dynein. Proc. Natl. Acad. Sci. USA 103:5741-5745.

[56] Mallik, R., B. C. Carter, S. A. Lex, S. J. King, and S. P. Gross. 2004. Cytoplasmic dynein functions as a gear in response to load. Nature 427:649-652.

[57] Kural, C., H. Kim, S. Syed, G. Goshima, V. I. Gelfand, and P. R. Selvin. 2005. Kinesin and dynein move a peroxisome in vivo: a tug-of-war or coordinated movement? Science 308:1469-1472.

[58] Hirakawa, E., H. Higuchi, and Y. Y. Toyoshima. 2000. Processive movement of single 22S dynein molecules occurs only at low ATP concentrations. Proc. Natl. Acad. Sci. USA 97:2533-2537.

[59] McDonald, H. B., R. J. Stewart, and L. S. Goldstein. 1990. The kinesin-like ncd protein of Drosophila is a minus end-directed microtubule motor. Cell 63:1159-1165.

[60] Chandra, R., E. D. Salmon, H. P. Erickson, A. Lockhart, and S. A. Endow. 1993. Structural and functional domains of the Drosophila ncd microtubule motor protein. J. Biol. Chem. 268:9005-9013.

[61] Karabay, A., and R. A. Walker. 1999. Identification of microtubule binding sites in the Ncd tail domain. Biochemistry 38:1838-1849.

[62] Endow, S. A., R. Chandra, D. J. Komma, A. H. Yamamoto, and E. D. Salmon. 1994. Mutants of the Drosophila ncd microtubule motor protein cause centrosomal and spindle pole defects in mitosis. J. Cell Sci. 107 (Pt 4):859-867.

[63] Endow, S. A., S. Henikoff, and L. Soler-Niedziela. 1990. Mediation of meiotic and early mitotic chromosome segregation in Drosophila by a protein related to kinesin. Nature 345:81-83.

[64] Hatsumi, M., and S. A. Endow. 1992. Mutants of the microtubule motor protein, nonclaret disjunctional, affect spindle structure and chromosome movement in meiosis and mitosis. J. Cell Sci. 101 (Pt 3):547-559.

[65] deCastro, M. J., R. M. Fondecave, L. A. Clarke, C. F. Schmidt, and R. J. Stewart. 2000. Working strokes by single molecules of the kinesin-related microtubule motor ncd. Nat. Cell Biol. 2:724-729.

[66] Foster, K. A., and S. P. Gilbert. 2000. Kinetic studies of dimeric Ncd: evidence that Ncd is not processive. Biochemistry 39:1784-1791.

[67] Pechatnikova, E., and E. W. Taylor. 1999. Kinetics processivity and the direction of motion of Ncd. Biophys. J. 77:1003-1016.

[68] Furuta, K., and Y. Y. Toyoshima. 2008. Minus-end-directed motor Ncd exhibits processive movement that is enhanced by microtubule bundling in vitro. Curr. Biol. 18:152-157.

[69] Diez, S., J. H. Helenius, and J. Howard. 2004. Biomolecular motors operating in engineered environments. In Nanobiotechnology: Concepts, Applications and Perspectives. C. M. Niemeyer, and C. A. Mirkin, editors. Wiley-VCH, Weinheim. 185-199.

[70] Kinosita, K., Jr., R. Yasuda, H. Noji, S. Ishiwata, and M. Yoshida. 1998. F1-ATPase: a rotary motor made of a single molecule. Cell 93:21-24.

[71] Kinosita, K., Jr., R. Yasuda, H. Noji, and K. Adachi. 2000. A rotary molecular motor that can work at near 100% efficiency. Philos. Trans. R. Soc. Lond., Ser. B: Biol. Sci. 355:473-489.

[72] Soong, R. K., G. D. Bachand, H. P. Neves, A. G. Olkhovets, H. G. Craighead, and C. D. Montemagno. 2000. Powering an inorganic nanodevice with a biomolecular motor. Science 290:1555-1558.

[73] Hess, H. 2006. Self-assembly driven by molecular motors. Soft Matter 2:669-677.

[74] Dinu, C. Z., D. B. Chrisey, S. Diez, and J. Howard. 2007. Cellular motors for molecular manufacturing. Anat. Rec. (Hoboken) 290:1203-1212.

[75] Suzuki, H., A. Yamada, K. Oiwa, H. Nakayama, and S. Mashiko. 1997. Control of actin moving trajectory by patterned poly(methyl methacrylate) tracks. Biophys. J. 72:1997-2001.

[76] Hess, H., J. Clemmens, D. Qin, J. Howard, and V. Vogel. 2001. Light-controlled molecular shuttles made from motor proteins carrying cargo on engineered surfaces. Nano Lett. 1:235-239.

[77] Riveline, D., A. Ott, F. Julicher, D. A. Winkelmann, O. Cardoso, J. J. Lacapere, S. Magnusdottir, J. L. Viovy, L. Gorre-Talini, and J. Prost. 1998. Acting on actin: the electric motility assay. Eur. Biophys. J. 27:403-408.

[78] Reuther, C., L. Hajdo, R. Tucker, A. A. Kasprzak, and S. Diez. 2006. Biotemplated nanopatterning of planar surfaces with molecular motors. Nano Lett. 6:2177-2183.

[79] van den Heuvel, M. G. L., M. P. De Graaff, and C. Dekker. 2006. Molecular sorting by electrical steering of microtubules in kinesin-coated channels. Science 312:910-914.

[80] Hutchins, B. M., M. Platt, W. O. Hancock, and M. E. Williams. 2007. Directing transport of CoFe2O4-functionalized microtubules with magnetic fields. Small 3:126-131.

[81] Stracke, P., K. J. Bohm, J. Burgold, H. J. Schacht, and E. Unger. 2000. Physical and technical parameters determining the functioning of a kinesin-based cell-free motor system. Nanotechnology 11:52-56.

[82] Gast, F. U., P. S. Dittrich, P. Schwille, M. Weigel, M. Mertig, J. Opitz, U. Queitsch, S. Diez, B. Lincoln, F. Wottawah, S. Schinkinger, J. Guck, J. Kas, J. Smolinski, K. Salchert, C. Werner, C. Duschl, M. S. Jager, K. Uhlig, P. Geggier, and S. Howitz. 2006. The microscopy cell (MicCell), a versatile modular flowthrough system for cell biology, biomaterial research, and nanotechnology. Microfluid. Nanofluid. 2:21-36.

[83] Tucker, R., P. Katira, and H. Hess. 2008. Herding nanotransporters: localized activation via release and sequestration of control molecules. Nano Lett. 8:221-226.

[84] Ionov, L., M. Stamm, and S. Diez. 2006. Reversible switching of microtubule motility using thermoresponsive polymer surfaces. Nano Lett. 6:1982-1987.

[85] Diez, S., C. Reuther, C. Dinu, R. Seidel, M. Mertig, W. Pompe, and J. Howard. 2003. Stretching and transporting DNA molecules using motor proteins. Nano Lett. 3:1251-1254.

[86] Dinu, C. Z., J. Opitz, W. Pompe, J. Howard, M. Mertig, and S. Diez. 2006. Parallel manipulation of bifunctional DNA molecules on structured surfaces using kinesin-driven microtubules. Small 2:1090-1098.

[87] Bachand, G. D., S. B. Rivera, A. K. Boal, J. Gaudioso, J. Liu, and B. C. Bunker. 2004. Assembly and transport of nanocrystal CdSe quantum dot

nanocomposites using microtubules and kinesin motor proteins. Nano Lett. 4:817-821.

[88] Bachand, G. D., S. B. Rivera, A. Carroll-Portillo, H. Hess, and M. Bachand. 2006. Active capture and transport of virus particles using a biomolecular motor-driven, nanoscale antibody sandwich assay. Small 2:381-385.

[89] Kikushima, K., and R. Kamiya. 2008. Clockwise translocation of microtubules by flagellar inner-arm dyneins in vitro. Biophys. J. 94:4014-4019.

[90] Anderson, C. M., G. N. Georgiou, I. E. Morrison, G. V. Stevenson, and R. J. Cherry. 1992. Tracking of cell surface receptors by fluorescence digital imaging microscopy using a charge-coupled device camera. Low-density lipoprotein and influenza virus receptor mobility at 4 degrees C. J. Cell Sci. 101 (Pt 2):415-425.

[91] Schutz, G. J., H. Schindler, and T. Schmidt. 1997. Single-molecule microscopy on model membranes reveals anomalous diffusion. Biophys. J. 73:1073-1080.

[92] Cheezum, M. K., W. F. Walker, and W. H. Guilford. 2001. Quantitative comparison of algorithms for tracking single fluorescent particles. Biophys. J. 81:2378-2388.

[93] Thompson, R. E., D. R. Larson, and W. W. Webb. 2002. Precise nanometer localization analysis for individual fluorescent probes. Biophys. J. 82:2775-2783.

[94] Ober, R. J., S. Ram, and E. S. Ward. 2004. Localization accuracy in single-molecule microscopy. Biophys. J. 86:1185-1200.

[95] Leduc, C., F. Ruhnow, J. Howard, and S. Diez. 2007. Detection of fractional steps in cargo movement by the collective operation of kinesin-1 motors. Proc. Natl. Acad. Sci. USA 104:10847-10852.

[96] Betzig, E., G. H. Patterson, R. Sougrat, O. W. Lindwasser, S. Olenych, J. S. Bonifacino, M. W. Davidson, J. Lippincott-Schwartz, and H. F. Hess. 2006. Imaging intracellular fluorescent proteins at nanometer resolution. Science 313:1642-1645.

[97] Rust, M. J., M. Bates, and X. Zhuang. 2006. Sub-diffraction-limit imaging by stochastic optical reconstruction microscopy (STORM). Nat. Methods 3:793-795.

[98] Watanabe, T. M., T. Sato, K. Gonda, and H. Higuchi. 2007. Three-dimensional nanometry of vesicle transport in living cells using dual-focus imaging optics. Biochem. Biophys. Res. Commun. 359:1-7.

[99] Toprak, E., H. Balci, B. H. Blehm, and P. R. Selvin. 2007. Three-dimensional particle tracking via bifocal imaging. Nano Lett. 7:2043-2045.

[100] Lambacher, A., and P. Fromherz. 1996. Fluorescence interference-contrast microscopy on oxidized silicon using a monomolecular dye layer. Appl. Phys. A 63:207-216.

[101] Kerssemakers, J., J. Howard, H. Hess, and S. Diez. 2006. The distance that kinesin-1 holds its cargo from the microtubule surface measured by fluorescence interference contrast microscopy. Proc. Natl. Acad. Sci. USA 103:15812-15817.

[102] Chan, W. C., D. J. Maxwell, X. Gao, R. E. Bailey, M. Han, and S. Nie. 2002. Luminescent quantum dots for multiplexed biological detection and imaging. Curr. Opin. Biotechnol. 13:40-46.

[103] Michalet, X., F. F. Pinaud, L. A. Bentolila, J. M. Tsay, S. Doose, J. J. Li, G. Sundaresan, A. M. Wu, S. S. Gambhir, and S. Weiss. 2005. Quantum dots for live cells, in vivo imaging, and diagnostics. Science 307:538-544.

[104] Johnson, C. J., N. Zhukovsky, A. E. Cass, and J. M. Nagy. 2008. Proteomics, nanotechnology and molecular diagnostics. Proteomics 8:715-730.

[105] Hohng, S., and T. Ha. 2004. Near-complete suppression of quantum dot blinking in ambient conditions. J. Am. Chem. Soc. 126:1324-1325.

[106] Nitzsche, B., F. Ruhnow, and S. Diez. 2008. Quantum-dot-assisted characterization of microtubule rotations during cargo transport. Nat. Nanotechnol. 3:552-556.

[107] Chang, Y. R., H. Y. Lee, K. Chen, C. C. Chang, D. S. Tsai, C. C. Fu, T. S. Lim, Y. K. Tzeng, C. Y. Fang, C. C. Han, H. C. Chang, and W. Fann. 2008. Mass production and dynamic imaging of fluorescent nanodiamonds. Nat. Nanotechnol. 3:284-288.

[108] Hyman, A. A., D. Chretien, I. Arnal, and R. H. Wade. 1995. Structural changes accompanying GTP hydrolysis in microtubules: information from a slowly hydrolyzable analogue guanylyl-(alpha,beta)-methylene-diphosphonate. J. Cell Biol. 128:117-125.

[109] Andreu, J. M., J. Bordas, J. F. Diaz, J. Garcia de Ancos, R. Gil, F. J. Medrano, E. Nogales, E. Pantos, and E. Towns-Andrews. 1992. Low resolution structure of microtubules in solution. Synchrotron X-ray scattering and electron microscopy of taxol-induced microtubules assembled from purified tubulin in comparison with glycerol and MAP-induced microtubules. J. Mol. Biol. 226:169-184.

[110] Arnal, I., and R. H. Wade. 1995. How does taxol stabilize microtubules? Curr. Biol. 5:900-908.

[111] Diaz, J. F., J. M. Valpuesta, P. Chacon, G. Diakun, and J. M. Andreu. 1998. Changes in microtubule protofilament number induced by Taxol binding to an easily accessible site. Internal microtubule dynamics. J. Biol. Chem. 273:33803-33810.

[112] Mansson, A., M. Sundberg, M. Balaz, R. Bunk, I. A. Nicholls, P. Omling, S. Tagerud, and L. Montelius. 2004. In vitro sliding of actin filaments labelled with single quantum dots. Biochem. Biophys. Res. Commun. 314:529-534.

[113] Vitre, B., F. M. Coquelle, C. Heichette, C. Garnier, D. Chretien, and I. Arnal. 2008. EB1 regulates microtubule dynamics and tubulin sheet closure in vitro. Nat. Cell Biol. 10:415-421.

[114] Wade, R. H., and D. Chretien. 1993. Cryoelectron microscopy of microtubules. J. Struct. Biol. 110:1-27.

[115] Thorn, K. S., J. A. Ubersax, and R. D. Vale. 2000. Engineering the processive run length of the kinesin motor. J. Cell Biol. 151:1093-1100.

[116] Wang, Z., and M. P. Sheetz. 2000. The C-terminus of tubulin increases cytoplasmic dynein and kinesin processivity. Biophys. J. 78:1955-1964.

[117] Lakamper, S., and E. Meyhofer. 2005. The E-hook of tubulin interacts with kinesin's head to increase processivity and speed. Biophys. J. 89:3223-3234.

[118] Mandelkow, E. M., M. Herrmann, and U. Ruhl. 1985. Tubulin domains probed by limited proteolysis and subunit-specific antibodies. J. Mol. Biol. 185:311-327.

[119] Bhattacharyya, B., D. L. Sackett, and J. Wolff. 1985. Tubulin, hybrid dimers, and tubulin S. Stepwise charge reduction and polymerization. J. Biol. Chem. 260:10208-10216.

[120] Block, S. M., C. L. Asbury, J. W. Shaevitz, and M. J. Lang. 2003. Probing the kinesin reaction cycle with a 2D optical force clamp. Proc. Natl. Acad. Sci. USA 100:2351-2356.

[121] Toba, S., T. M. Gibson, K. Shiroguchi, Y. Y. Toyoshima, and D. J. Asai. 2004. Properties of the full-length heavy chains of Tetrahymena ciliary outer arm dynein separated by urea treatment. Cell Motil. Cytoskeleton 58:30-38.

[122] Wada, Y., T. Hamasaki, and P. Satir. 2000. Evidence for a novel affinity mechanism of motor-assisted transport along microtubules. Mol. Biol. Cell 11:161-169.

[123] Yao, J., D. R. Larson, H. D. Vishwasrao, W. R. Zipfel, and W. W. Webb. 2005. Blinking and nonradiant dark fraction of water-soluble quantum dots in aqueous solution. Proc. Natl. Acad. Sci. USA 102:14284-14289.

[124] Endres, N. F., C. Yoshioka, R. A. Milligan, and R. D. Vale. 2006. A lever-arm rotation drives motility of the minus-end-directed kinesin Ncd. Nature 439:875-878.

[125] Hunter, A. W., M. Caplow, D. L. Coy, W. O. Hancock, S. Diez, L. Wordeman, and J. Howard. 2003. The kinesin-related protein MCAK is a microtubule depolymerase that forms an ATP-hydrolyzing complex at microtubule ends. Mol. Cell 11:445-457.

[126] Hancock, W. O., and J. Howard. 1998. Processivity of the motor protein kinesin requires two heads. J. Cell Biol. 140:1395-1405.

[127] Papra, A., N. Gadegaard, and N. B. Larsen. 2001. Characterization of ultrathin poly(ethylene glycol) monolayers on silicon substrates. Langmuir 17:1457-1460.

Acknowledgements

I am grateful for the support of many people, who were involved in one or the other way in the work presented here. This is the opportunity to thank them and I am doing so with great pleasure.

Almost 4 years ago I was fortunate enough to join the rapidly developing young group lead by Dr. Stefan Diez with real enthusiasm. He was the perfect person to supervise my work. In particular, I have learnt almost everything that I know about optical microscopy from him. What I am especially grateful for as well is that he gave me all the freedom to explore my topic, but was always there when I needed advise.

Prof. Dr. Jonathon Howard and Prof. Dr. Wolfgang Pompe were co-supervising my work. I was lucky to benefit from their vast experience and knowledge. Their advise helped me to discover new aspects of my project, which I found very enriching.

An integral part of my work was the excellent tracking software developed by Felix Ruhnow and David Zwicker. They both did a great job in implementing this software and always found a way to incorporate additional features from my endless list of wishes.

The kind gifts of 22S dynein from Yuuko Wada and Peter Satir (Albert Einstein College of Medicine of Yeshiva University, New York, USA), and ncd from Lukasz Hajdo and Andrzej A. Kasprzak (Nencki Institute Warsaw, Poland) opened new exciting possibilities for my work.

When I started my project, I did not know much about FLIC microscopy. Dr. Jacob Kerssemakers shared his experience in FLIC microscopy and introduced me to the technique. Unforgotten are the caffeine intake sessions, most of the time bringing about exceptionally fruitful discussions.

I experienced a lot of technical support from Corina Bräuer and Dr. Doreen Naumburger. Their reliable assistance has often made life much less stressful for me.

When writing this thesis I tried to make my research reasonably accessible to the reader. Then it is wonderful to have people like Till Korten

and my brother Tilo around, who helped me to get my ideas straight. Owing to their critical reading of and commenting on the manuscript, this work has improved a lot.

Franziska Friedrich has created the beautiful and illustrative schematic 3-D drawings of motility assays used in this work.

The fantastic working conditions that I experienced are to a great extend due to the members of the research groups of Dr. Stefan Diez and of Prof. Dr. Jonathon Howard. As far as I have not already done so above I would like to thank all these people - particularly Dr. Cecile Leduc, Dr. Jonne Helenius, Dr. Gary Brouhard, Samaneh Mashaghi, Till Korten and Gero Fink - for help and for many inspiring and moreover pleasant discussions.

I am also very grateful for the support of my family. Particularly, I appreciate Sandra’s (mostly successful) attempts to cheer me up whenever necessary.